Synaptopodin regulates denervation-induced plasticity at hippocampal mossy fiber synapses

Pia Kruse[1], Gudrun Brandes[2], Hanna Hemeling[1], Zhong Huang[2], Christoph Wrede[3,4], Jan Hegermann[3,4], Andreas Vlachos[1,5,6,§], Maximilian Lenz[1,2,§]

[1]Department of Neuroanatomy, Institute of Anatomy and Cell Biology, Faculty of Medicine, University of Freiburg, Freiburg, Germany.

[2]Hannover Medical School, Institute of Neuroanatomy and Cell Biology, Hannover, Germany.

[3]Hannover Medical School, Institute of Functional and Applied Anatomy, Hannover, Germany.

[4]Hannover Medical School, Research Core Unit Electron Microscopy, Hannover, Germany.

[5]Center for Basics in Neuromodulation (NeuroModulBasics), Faculty of Medicine, University of Freiburg, Freiburg, Germany.

[6]Center BrainLinks-BrainTools, University of Freiburg, Freiburg, Germany.

[§]Correspondence to andreas.vlachos@anat.uni-freiburg.de and lenz.maximilian@mh-hannover.de, Department of Neuroanatomy, Institute of Anatomy and Cell Biology, Faculty of Medicine, University of Freiburg, 79104 Freiburg, Germany and Hannover Medical School, Institute of Neuroanatomy and Cell Biology, Carl-Neuberg-Straße 1, 30625 Hannover, Germany.

Keywords: lesion-induced plasticity, denervation, synaptopodin, local protein synthesis

ABSTRACT

Neurological diseases can lead to the denervation of brain regions caused by demyelination, traumatic injury or cell death. Nevertheless, the molecular and structural mechanisms underlying lesion-induced reorganization of denervated brain regions are a matter of ongoing investigation. In order to address this issue, we performed an entorhinal cortex lesion (ECL) in mouse organotypic entorhino-hippocampal tissue cultures of both sexes and studied denervation-induced plasticity of mossy fiber synapses, which connect dentate granule cells (dGCs) with CA3 pyramidal cells (CA3-PCs) and play important roles in spatial learning. Partial denervation caused a strengthening of excitatory neurotransmission in dGCs, in CA3-PCs, and their direct synaptic connections as revealed by paired recordings (GC-to-CA3). These functional changes were accompanied by ultrastructural reorganization of mossy fiber synapses, which regularly contain the plasticity-related protein synaptopodin and the spine apparatus organelle. We demonstrate that the spine apparatus organelle and its integral protein synaptopodin are associated with ribosomes in close proximity to synaptic sites and unravel a synaptopodin-related transcriptome. Notably, synaptopodin-deficient tissue preparations that lack the spine apparatus organelle, failed to express lesion-induced synaptic adjustments. Hence, synaptopodin and the spine apparatus organelle play a crucial role in regulating lesion-induced synaptic plasticity at hippocampal mossy fiber synapses.

INTRODUCTION

Denervation is a common feature of various neurological diseases, which are accompanied by neuronal cell death, demyelination or traumatic injury of the central nervous system (Mesulam et al., 2019). As a result of the loss-of-input in otherwise healthy brain regions, complex reorganizational processes of neural circuits have been described. Specifically, excitatory synaptic strengthening upon denervation or activity deprivation has been reported as a compensatory synaptic adjustment (Turrigiano et al., 1998; Riegle and Meyer, 2007). However, the mechanisms that mediate lesion-induced synaptic plasticity at local dendritic sites warrant further investigation.

The hippocampal network is a crucial structure in memory acquisition. Here, the excitatory connection between dentate granule cells (dGCs) and CA3 pyramidal cells (CA3-PCs), i.e., the hippocampal mossy fiber synapse, has been demonstrated to play a crucial role in memory formation, maintenance and retrieval (Weng et al., 2018). Although numerous studies have addressed the plasticity features of this synapse (e.g. the detonating transmission; (Lee et al., 2013)) and its impact on memory and behavior, no studies have addressed whether lesion-induced synaptic plasticity occurs at this synapse when the main cortical excitatory input is affected. Organotypic tissue cultures of the entorhino-hippocampal complex provide the opportunity to study synaptic transmission at hippocampal mossy fiber synapses in a steady-state condition (Maus et al., 2020). Based on the lamination of cortico-hippocampal inputs, the *in vitro* entorhinal-cortex lesion can be used to explore the effects of partial denervation on hippocampal neural circuits (Prang et al., 2003; Vlachos et al., 2012a; Vlachos et al., 2012c; Lenz et al., 2019).

In this study we used an entorhinal cortex lesion (ECL) of organotypic entorhino-hippocampal tissue cultures to study synaptic adaptations in the dentate gyrus and CA3 network upon partial denervation. We provide evidence that partial denervation leads to ultrastructural changes and excitatory synaptic strengthening in both dGCs and CA3-PCs. Using paired whole-cell patch-clamp recordings, we demonstrate changes in synaptic transmission at hippocampal mossy fiber synapses that are accompanied by ultrastructural reorganizations of the plasticity-related spine apparatus organelle (Deller et al., 2003; Jedlicka et al., 2009; Vlachos et al., 2009; Vlachos et al., 2013; Korkotian et al., 2014; Jedlicka and Deller, 2017; Maggio and Vlachos, 2018; Lenz et al., 2021a; Lenz et al., 2021b). Our data suggest that synaptopodin and the spine apparatus organelle associate with dendritic ribosomes that could be crucial for the local implementation of lesion-induced synaptic plasticity (Sutton et al., 2006). Consequently, synaptopodin-deficient tissue cultures, which lack the spine apparatus organelle, showed alterations in their ability to express lesion-induced plasticity of excitatory synapses and the region-specific transcriptome. We therefore conclude, that the spine apparatus organelle is essential for regulating lesion-induced plasticity, which might be linked to ribosomal associations near synaptic sites.

MATERIALS AND METHODS

Ethics statement

Mice were maintained in a 12 h light/dark cycle with food and water available ad libitum. Every effort was made to minimize distress and pain of animals. All experimental procedures were performed according to German animal welfare legislation and approved by the appropriate animal welfare committee and the animal welfare officer of Albert-Ludwigs-University Freiburg, Faculty of Medicine (X-17/07K, X-17/09K, X-21/01B) and Hannover Medical School (2022/308).

Preparation of tissue cultures

Entorhino-hippocampal tissue cultures were prepared at postnatal day 3-5 from C57BL/6J (wildtype, Synpo$^{+/+}$) and B6.129-Synpo^{tm1Mndl}/Dllr [Synpo$^{-/-}$, (Deller et al., 2003; Lenz et al., 2021a; Lenz et al., 2021b)] mice of either sex as previously described (Del Turco and Deller, 2007). Synpo$^{-/-}$ strain was back crossed for at least 10 times to establish C57BL/6J genetic background. Cultivation medium contained 50% (v/v) MEM, 25% (v/v) basal medium eagle, 25% (v/v) heat-inactivated normal horse serum, 25 mM HEPES buffer solution, 0.15% (w/v) bicarbonate, 0.65% (w/v) glucose, 0.1 mg/ml streptomycin, 100 U/ml penicillin, and 2 mM glutamax. The pH was adjusted to 7.3. All tissue cultures were allowed to mature for at least 18 days in a humidified atmosphere with 5% CO_2 at 35°C. Cultivation medium was replaced 3 times per week.

Entorhinal cortex lesion (ECL)

The entorhinal cortex of mature slice cultures (≥18 days *in vitro*) was transected with a sterile scalpel from the rhinal to the hippocampal fissure to achieve a complete lesion of the perforant path. Except for the lesion-induced partial denervation of the hippocampus, cytoarchitecture of both the hippocampus and the entorhinal cortex remained unchanged.

Whole-cell patch-clamp recordings

Whole-cell patch-clamp recordings were carried out at 35°C (3-6 neurons per culture). The bath solution contained (in mM) 126 NaCl, 2.5 KCl, 26 $NaHCO_3$, 1.25 NaH_2PO_4, 2 $CaCl_2$, 2 $MgCl_2$, and 10 glucose (aCSF) and was oxygenated continuously (5% CO_2 / 95% O_2). Patch pipettes contained (in mM) 126 K-gluconate, 10 HEPES, 4 KCl, 4 ATP-Mg, 0.3 GTP-Na_2, 10 PO-Creatine, 0.3% (w/v) biocytin (pH 7.25 with KOH, 290 mOsm with sucrose), having a tip resistance of 4-6 MΩ. Neurons were visually identified using a LN-Scope (Luigs & Neumann) equipped with an infrared dot-contrast and a 40x water-immersion objective (NA 0.8; Olympus). Spontaneous excitatory postsynaptic currents (sEPSCs) of both dGCs and CA3-PCs were recorded in voltage-clamp mode at a holding potential of −70 mV. In the dentate gyrus, recordings were performed in granule cells at the outer parts of the granule cell layer in the suprapyramidal blade with maximum distance to the subgranular zone. Moreover, the resting membrane potential was estimated before our recordings to exclude immature granule cells. In CA3,

recordings were performed in pyramidal cells close to the dentate gyrus in proximity to str. lucidum. Series resistance was monitored before and after each recording and recordings were discarded if the series resistance reached ≥ 30 MΩ. For recording of intrinsic cellular properties in current-clamp mode, pipette capacitance of 2.0 pF was corrected and series resistance was compensated using the automated bridge balance tool of the MultiClamp commander. I-V-curves were generated by injecting 1 s square pulse currents starting at −100 pA and increasing in 10 pA steps until +500 pA current injection was reached (sweep duration: 2 s).

Paired whole-cell patch-clamp recordings of hippocampal mossy fiber synapses

Action potentials were generated in the presynaptic dGC by 5 ms square current pulses (1 nA). For connectivity analysis, 5 action potentials were applied at 20 Hz respectively (inter-sweep-interval: 10 s; at least 30 repetitions), while recording unitary excitatory postsynaptic currents (uEPSCs) from CA3-PCs. Neurons were considered to be connected if > 5 % of action potentials evoked time-locked inward uEPSCs (Vlachos et al., 2012b). Recordings were performed in the presence of (-)-bicuculline-methiodide (10 µM, Abcam, #ab120108) to prevent inhibitory synapse recruitment. Moreover, glutamine (200 µM, Gibco, #11539876) was added to the recording medium to avoid synapse depletion (Tani et al., 2014).

Post-hoc staining and imaging

Tissue cultures were fixed overnight in a solution of 4% (w/v) paraformaldehyde (PFA; in PBS (0.1M, pH 7.4) with 4% (w/v) sucrose). After fixation, cultures were washed in PBS (0.1 M, pH 7.4) and consecutively incubated for 1 h with 10% (v/v) normal goat serum (NGS) in 0.5% (v/v) Triton X-100 containing PBS to reduce nonspecific staining. For post-hoc visualization of patched dGCs and CA3-PCs, Streptavidin Alexa Fluor 488 (Streptavidin A488, 1:1000; Invitrogen, #S32354) was added to the incubation solution. DAPI nuclear stain (1:5000 in PBS for 10 min; Thermo Scientific, #62248) was used to visualize cytoarchitecture. Cultures were washed, transferred onto glass slides and mounted for visualization with DAKO anti-fading mounting medium (Agilent, #S302380-2).

Serial block-face scanning electron microscopy (SBF-SEM)

For volume electron microscopic evaluation, samples were fixed in 1.5 % glutaraldehyde and 1.5 % paraformaldehyde buffered in 0.15 M HEPES, pH = 7.35. Further processing was already described previously (Beike et al., 2019) based on accessible protocols (https://ncmir.ucsd.edu/sbem-protocol). In brief, for postfixation and staining reduced osmium tetroxide, thiocarbohydrazide and osmium tetroxide (rOTO), followed by uranyl acetate and lead aspartate were applied. After dehydration in an ascending acetone series, samples were embedded in epoxy resin, Araldite CY212 premix kit (Agar Scientific, Stansted Essex, UK).

118 Target regions were identified on semithin sections (1 µm, stained with toluidine blue). Accordingly,
119 resin blocks were trimmed, mounted with conductive epoxy glue (Chemtronics, CircuitWorks,
120 Kennesaw, USA) on sample pin stubs (Micro to Nano, Haarlem, Netherlands), precisely trimmed again
121 and sputter coated with a gold layer.
122 Image stacks were acquired with a Zeiss Merlin VP Compact SEM (Carl Zeiss Microscopy GmbH,
123 Oberkochen, Germany) equipped with a Gatan 3View2XP system (Gatan Inc., Pleasanton, CA, USA).
124 Every second block-face (section thickness 50 nm) was scanned with 3.5 kV acceleration voltage and
125 100 % focal charge compensation (10 nm pixel size, 3 µs dwell time) by using the Multi-ROI mode to
126 record multiple areas on each surface.

127 **Transmission electron microscopy – mossy fiber synapse visualization**

128 Wildtype (Synpo$^{+/+}$) and Synpo$^{-/-}$ tissue cultures were fixed in 4 % paraformaldehyde (w/v) and 2 %
129 glutaraldehyde (w/v) in 0.1 M phosphate buffer (PB) overnight and washed for 1 hour in 0.1 M PB.
130 After fixation, tissue cultures were sliced with a vibratome and the slices were incubated with 1 %
131 osmium tetroxide for 20 min in 5 % (w/v) sucrose containing 0.1 M PB. The slices were washed 5 times
132 for 10 min in 0.1 M PB and washed in graded ethanol [10 min in 10 % (v/v) and 10 min in 20 % (v/v)].
133 The slices were then incubated with uranyl acetate [1 % (w/v) in 70 % (v/v) ethanol] overnight and
134 were subsequently dehydrated in graded ethanol 80 % (v/v), 90 % (v/v) and 98 % (v/v) for 10 min.
135 Finally, slices were incubated with 100 % (v/v) ethanol twice for 15 min followed by two 15 min
136 washes with propylene oxide. The slices were then transferred for 30 min in a 1:1 mixture of
137 propylene oxide with durcupan and then for 1 hour in durcupan. The durcupan was exchanged with
138 fresh durcupan and the slices were transferred to 4 °C overnight. The slices were then embedded
139 between liquid release-coated slides and coverslips. Cultures were re-embedded in blocks and ultrathin
140 sections were collected on copper grids, at which point an additional Pb-citrate contrasting step was
141 performed (3 min). Electron microscopy was performed at a LEO 906E microscope (Zeiss) at 4646x
142 magnification.

143 **Synaptopodin co-Immunoprecipitation (SP-coIP), RNA-Seq analysis and negative contrast**
144 **electron microscopy**

145 Six tissue cultures per biological replicate were washed in coIP-solution and dounce homogenized on
146 ice in a solution containing (150 µl per sample, coIP-solution, in mM): 10 HEPES, 120 NaCl, 0.05%
147 (v/v) NP-40 or IGEPAL CA-630 (Sigma Aldrich, #I8896), cOmplete protease inhibitor (Roche,
148 according to manufacturer's instructions), murine RNase inhibitor (1:1000, New England Biolabs,
149 #M0314) and cycloheximide (0.5 mg/ml, Sigma Aldrich, #C-4859). Input was precleared twice with
150 protein A beads (10 µl per 100 µl sample/supernatant) to reduce non-specific binding. Protein A beads
151 (10 µl, New England Biolabs, #S1425) were washed twice in coIP-solution and consecutively incubated
152 for 1 hour at 4°C with an anti-synaptopodin antibody (rabbit anti-Synaptopodin, Synaptic Systems,

153 #163002). Beads were carefully washed twice to remove unbound antibodies and incubated for 1 hour
154 with the precleared supernatant ('input') at 4 °C with head-over-tail rotation. 10 µl of the precleared
155 supernatant were kept as input control. After incubation, beads were washed twice with coIP-solution
156 and finally dissolved in RNA protection buffer (New England Biolabs).
157 In another round of experiments, hippocampal tissue from adult animals was used for co-
158 immunoprecipitation experiments (antibody: monoclonal rabbit anti-synaptopodin, Abcam, #ab259976
159 Abcam) with subsequent negative contrast electron microscopy. Beads (30 µl) were adsorbed on carbon-
160 coated films stabilized by a copper grid and stained with 3% uranyl acetate (Serva, Heidelberg,
161 Germany). Samples were immediately examined with a transmission electron microscope (Morgagni
162 268, 80 kV, FEI, Eindhoven, The Netherlands).
163 RNA was released from the beads through protein K lysis (Monarch® Total RNA Miniprep Kit; New
164 England Biolabs, #T2010S). After lysis, beads were removed from the solution in a magnetic rack and
165 the RNA containing supernatant was transferred to fresh tubes. RNA isolation on coIP- and input-
166 samples was then performed according to the manufacturer's instructions. RNA content was determined
167 using the Agilent RNA 6000 Pico Kit (Agilent, #5067-1513) with a 2100 Bioanalyzer (Agilent,
168 #G2939BA). RNA Library preparations for Synpo-related transcriptome analysis were performed using
169 the NEBNext® Single Cell/Low Input RNA Library Prep Kit for Illumina® (New England Biolabs,
170 #E6420) according to the manufacturer's instructions. We quantified the libraries using the NEBNext
171 Library Quant Kit for Illumina (New England Biolabs, #E7630) based on the mean insert size provided
172 by the Bioanalyzer. A 10 nM sequencing pool (120 µl in Tris-HCl, pH 8.5) was generated for sequencing
173 on the NovaSeq6000 Sequencing platform (Illumina; service provided by CeGaT GmbH, Tübingen,
174 Germany). We performed a paired-end sequencing with 150 bp read length. Data analysis was
175 performed at the Galaxy platform (usegalaxy.eu). All files contained more than 10 M high-quality reads
176 (after mapping to the reference genome; mm10) having at least a phred quality of 30 (> 90 % of total
177 reads).

178 **Regional mRNA library preparations and transcriptome analysis**

179 RNA Library preparations for transcriptome analysis were performed using the NEBNext® Single
180 Cell/Low Input RNA Library Prep Kit for Illumina® (New England Biolabs, #E6420) according to the
181 manufacturer's instructions. Briefly, isolation of the dentate gyrus and CA3 area from individual tissue
182 cultures was performed using a scalpel. One isolated dentate gyrus or CA3 area respectively was
183 transferred to 7.5 µl lysis buffer (supplemented with murine RNase inhibitor) and homogenized using a
184 pestle. Samples were centrifuged for 30 s at 10,000 g and 5 µl of supernatant were collected from
185 individual samples and further processed. After cDNA synthesis, cDNA amplification was performed
186 according to the manufacturer's protocol with 12 PCR cycles. cDNA yield was consecutively analyzed
187 by a High Sensitivity DNA assay on a Bioanalyzer instrument (Agilent). cDNA amount was adjusted
188 to 10 ng for further downstream applications. After fragmentation and adaptor ligation, dual index

189 primers (New England Biolabs, #E7600S) were ligated in a library amplification step using 10 PCR
190 cycles. Libraries were finally cleaned up with 0.8X SPRI beads following a standard bead purification
191 protocol. Library purity and size distribution was assessed with a High Sensitivity DNA assay on a
192 Bioanalyzer instrument (Agilent). We quantified the libraries using the NEBNext Library Quant Kit for
193 Illumina (New England Biolabs, #E7630) based on the mean insert size provided by the Bioanalyzer. A
194 10 nM sequencing pool (120 µl in Tris-HCl, pH 8.5) was generated for sequencing on the NovaSeq6000
195 Sequencing platform (Illumina; service provided by CeGaT GmbH, Tübingen, Germany). We
196 performed a paired-end sequencing with 100 bp read length. Data analysis was performed at the Galaxy
197 platform (usegalaxy.eu). All files contained more than 10 M high-quality reads (after mapping to the
198 reference genome; mm10) having at least a phred quality of 30 (>90% of total reads).

199 **Quantification and statistics**

200 Electrophysiological data were analyzed using pClamp 10.7 (Axon Instruments) and MiniAnalysis
201 (Synaptosoft) software. The fraction of action potentials followed by time-locked excitatory
202 postsynaptic current responses was considered as synaptic response rate. uEPSC amplitude was assessed
203 in uEPSCs from successfully transmitted action potentials as well as the mean amplitude of all
204 successfully evoked postsynaptic responses. In order to ensure analysis of time-locked unitary
205 responses, events were included if > 5% of presynaptic pulses were successfully transmitted for each
206 pulse respectively. For individual pulses in pulse trains that caused ≤ 5% successfully transmitted
207 events, response rate was set to '0'. sEPSC properties were analyzed using the automated template
208 search tool for event detection. Since sEPSC kinetics might contain information on their synaptic origin
209 (in CA3-PCs, large EPSCs have been identified to originate from hippocampal mossy fibers (Henze et
210 al., 2002b)), we performed a hierarchical analysis of sEPSCs based on their amplitude. All events of a
211 recorded cell were sorted based on their peak amplitude. Events above the 50th percentile therefore
212 correspond to all events above the cells' median amplitude of events. Amplitude and half width data
213 from sEPSC analysis have been plotted to visualize sEPSC kinetics and linear fitting was employed to
214 detect changes in parameter interdependencies. sEPSC area was reported as a function of amplitude and
215 half width. Input resistance was calculated for the injection of –100 pA current at a time frame of 200
216 ms with a maximum distance to the initial hyperpolarization. Resting membrane potential was
217 calculated as the mean baseline value. AP detection was performed using the input-output curve
218 threshold search event detection tool, and the AP frequency was assessed by the number of APs detected
219 during the respective current injection time.
220 3D reconstructions of individual dendritic spines in electron micrograph image stacks were performed
221 using the TrakEM2 tool in the Fiji software environment by 3 individual investigators blind to
222 experimental conditions and hypothesis (Cardona et al., 2012). From one image stack, subfields were
223 selected (proximal to soma: dentate gyrus (DG), 10-50 µm; CA3, 30-90 µm distance to soma; distal to

224 soma: >100 µm distance to soma in both subfields) and all pre- and postsynaptic compartments of
225 asymmetric synapses that were fully captured on image stacks were manually reconstructed.
226 Transmission electron microscopy images of mossy fiber synapses were saved as TIF-files and analyzed
227 using the ImageSP Viewer software (http://e.informer.com/sys-prog.com). Ultrastructural features were
228 analyzed by an investigator blind to experimental conditions in randomly selected mossy fiber terminals
229 from electron micrographs of the stratum lucidum in non-lesioned and lesioned wildtype tissue cultures.
230 RNA sequencing data were uploaded to the Galaxy web platform (public server: usegalaxy.eu; (Goecks
231 et al., 2010; Afgan et al., 2018; Galaxy, 2022)) and transcriptome analysis was performed using the
232 Galaxy platform in accordance with the reference-based RNA-seq data analysis tutorial (Batut et al.,
233 2021). Adapter sequencing, low quality, and short reads were removed via the CUTADAPT tool. Reads
234 were mapped using RNA STAR with the mm10 full reference genome (Mus musculus). The evidence-
235 based annotation of the mouse genome (GRCm38), version M25 (Ensembl 100), served as gene model
236 (GENCODE). For an initial assessment of gene expression, unstranded FEATURECOUNT analysis
237 was performed from RNA STAR output. Only samples that contained >60% uniquely mapping reads
238 (feature: "exon") were considered for further analysis. Statistical evaluation was performed using
239 DESeq2 with "pathway integrity" (ECL experiments) or "coIP" (synaptopodin-coIP experiments) as
240 the primary factor that might affect gene expression. Genes with a low number of mean reads (< 300
241 BaseMean) were excluded from further analysis. Genes were considered as differentially expressed or
242 enriched if the adjusted p-value was < 0.05. Data visualization was performed according to a modified
243 version of a previously published workflow (Reimand et al., 2019). Further functional enrichment
244 analyses were performed using g:Profiler (version e107_eg54_p17_bf42210) with g:SCS multiple
245 testing correction method applying significance threshold of 0.05 (Raudvere et al., 2019). Gene sets
246 with 100-500 terms were considered for illustration. Heatmaps were generated based on z-scores of the
247 normalized count table.
248 For transcriptome analysis following synaptopodin-coIP, DESeq2 analysis was performed to compare
249 coIP and input samples. Differentially enriched genes in coIP ($p_{adj} < 0.05$ and log2(FC) > 0) were
250 considered for further analyses. To correct for non-specific antibody binding, DESeq2 output (log2(FC))
251 from the same experimental procedure in synaptopodin-deficient tissue cultures was subtracted from
252 from log2(FC) of differentially enriched genes in wildtype cultures. Only those differentially expressed
253 genes that showed > 30% enrichment in FC after Synpo-KO correction were considered as significantly
254 enriched.
255 Data were statistically analyzed using GraphPad Prism 7 or 9 (GraphPad software, USA). For statistical
256 comparison of two experimental groups, a Mann-Whitney test was employed. For statistical comparison
257 of three experimental groups, a Kruskal-Wallis test was employed. In the graphs demonstrating volumes
258 of the synaptic compartments, the box depicts 25-75 percentile, whiskers depict 10-90 percentile and
259 the line indicates the median. Values outside this range were indicated by individual dots. Otherwise,
260 values represent the mean ± standard error of the mean (s.e.m.). sEPSC amplitude/frequency plots and

AP-frequency plots were statistically assessed by the repeated measure (RM) two-way ANOVA test with Sidak's (two groups) multiple comparisons test. uEPSC amplitude values from individual cells were stacked in subcolumns and the pulse number was defining tabular rows (COLUMN factor: pathway integrity, genetic background; ROW factor: EPSC amplitude bin or current injection). P-values < 0.05 were considered statistically significant (*$p < 0.05$, **$p < 0.01$, ***$p < 0.001$); results that did not yield significant differences are designated 'ns'. Statistical differences in XY-plots were indicated in the legend of the figure panels (*) when detected through multiple comparisons, irrespective of their localization and the level of significance.

Data availability

Source files and detailed statistical analyses are available from the Dryad data repository (https://doi.org/10.5061/dryad.x0k6djhpc) using the following accession link: https://datadryad.org/stash/share/U3tRrrsNocTeYFGOxQb-Bc2OfhqxT2aWyuyPVw5WMI4. Sequencing data have been deposited in the Gene Expression Omnibus (GEO) repository (accession number: GSE216509). Original data are available from the authors upon reasonable request.

Digital illustrations

Confocal image stacks were stored as TIF files. Figures were prepared using the ImageJ software package (https://imagej.nih.gov/ij/) and Photoshop graphics software (Adobe, San Jose, CA, USA). Image brightness and contrast were adjusted.

RESULTS

Entorhinal cortex lesion leads to excitatory synaptic strengthening in both dGCs and CA3-PCs

Entorhinal cortex lesion was performed in mature tissue cultures to achieve a partial denervation of both dGCs and CA3-PCs (Figure 1A). Spontaneous excitatory postsynaptic currents (sEPSCs) were recorded from dGCs and CA3-PCs in non-lesioned control and lesioned tissue cultures (3 days post entorhinal cortex lesion, 3dp ECL) to assess denervation-induced effects on excitatory neurotransmission (Figure 1B). As previously described [e.g., (Vlachos et al., 2012c; Lenz et al., 2019)], partial denervation caused a strengthening of excitatory synapses in dGCs, i.e., a significant increase in both the mean sEPSC amplitude and half width as well as the mean sEPSC area (Figure 1C). Percentile analysis revealed that the lesion-induced increase in sEPSC amplitudes is evident when comparing the 50% biggest events in both groups while no effect was observed when comparing smaller events (Figure 1D). Notably, a significant upregulation in the mean sEPSC frequency was observed after lesion (Figure 1E) that resulted from an increased abundance of high amplitude sEPSCs as revealed by the amplitude/frequency-plot (Figure 1F).

Next, we examined excitatory neurotransmission in CA3-PCs in non-lesioned and lesioned cultures (3dp ECL; Figure 1G-J). Again, a significant increase in both the mean sEPSC amplitude and area was observed in CA3-PCs from lesioned cultures indicating a denervation-induced excitatory synaptic strengthening (Figure 1G). Notably, the mean sEPSC half width remained unchanged. In the sEPSC amplitude percentile analysis, excitatory synaptic strengthening seems to be restricted to the high amplitude events (Figure 1H). Moreover, the mean sEPSC frequency remained unchanged upon ECL (Figure 1I), which resulted from an increase in the abundance of high amplitude events at the expense of small amplitude events (Figure 1J, RM two-way ANOVA followed by Sidak's multiple comparisons test). We therefore conclude that ECL strengthens excitatory neurotransmission in both dGCs and CA3-PCs.

Partial denervation does not cause changes in intrinsic cellular properties

Passive and active membrane properties were assessed in both dGCs (Figure 2A, C, E) and CA3-PCs (Figure 2B, D, F) to test for adaptations of intrinsic cellular properties upon lesion. In dGCs no changes in passive membrane properties (Figure 2A), i.e., the resting membrane potential (RMP) and the input resistance as well as the input-output curve dynamics were observed (Figure 2C). Additionally, the action potential frequency of dGCs was similar in lesioned and non-lesioned cultures (Figure 2E). Noteworthy, RMP assessment confirmed the mature state of the recorded dGCs [c.f. (Strehl et al., 2018)].

Concerning CA3-PCs, neither the passive membrane properties (Figure 2D) – including input-output curve dynamics – nor the active properties (Figure 2F) were changed. Based on these results, we conclude that intrinsic cellular properties were stable following denervation in both tested cell types of the hippocampal network.

315 **Entorhinal cortex lesion induces ultrastructural changes in dendritic spines**
316 To visualize lesion-induced effects on the ultrastructural level in a time-dependent manner, we
317 performed 3D-electron microscopy (based on SBF-SEM) in both dentate gyrus (DG) and CA3 subfields
318 (Figure 3). Regions of interest were identified in image stacks from proximal (DG, 10-50 µm; CA3, 30-
319 90 µm distance to soma) and distal apical dendrites (>100 µm distance to soma in both subfields). 3D
320 reconstruction was performed in randomly selected areas in the region of interest and all synaptic
321 compartments of asymmetric spine synapses that were fully included in the image stacks were analyzed
322 in unlesioned control cultures and 2 hours (2hp ECL) as well as 3 days (3dp ECL) after entorhinal cortex
323 lesion (Figure 3A, F). In the DG, proximal dendrites that receive intrahippocampal inputs showed a
324 reduction in postsynaptic volume, while the presynaptic compartment remained unchanged (Figure 3B).
325 Interestingly, the complexity of synaptic organization, which was measured by the number of
326 postsynapses at the very same presynaptic bouton, increased constantly over time (Figure 3C). Distal
327 dendritic synapses showed a decline in both pre- and postsynaptic volumes upon lesion (Figure 3D),
328 while synaptic complexity remained unchanged.
329 In the CA3 subfield of proximal synapses, entorhinal cortex lesion caused an increase in presynaptic
330 volumes 3 days post lesion, while the postsynaptic volume remained stable (Figure 3G). In contrast,
331 distal dendritic synapses showed a decrease in postsynaptic volumes, while the presynaptic
332 compartment remained unchanged (Figure 3I). Here, synaptic complexity was unchanged in both
333 proximal and distal dendritic compartments (Figure 3H, J).

334 **Entorhinal cortex lesion induces changes in synaptic transmission at hippocampal mossy fiber**
335 **synapses**
336 Hippocampal mossy fiber synapses have been linked to learning processes and memory formation (Lipp
337 et al., 1988; Vandael et al., 2020). They are characterized by their generation of large postsynaptic
338 currents upon activation (Henze et al., 2002b). Given that our results hint towards a preferential lesion-
339 related plasticity induction in readily strong synapses of CA3-PCs, we next assessed the features of
340 synaptic transmission at hippocampal mossy fiber synapses.
341 Therefore, we performed paired whole-cell patch-clamp recordings of individual dGCs and CA3-PCs
342 in organotypic tissue cultures (Figure 4A). To test for synaptic connections, 5 consecutive action
343 potentials at 20 Hz frequency were elicited in dGCs (Figure 4B). Unitary excitatory postsynaptic
344 currents (uEPSCs) were monitored in CA3-PCs in non-lesioned and lesioned tissue cultures. We found
345 that a train of presynaptic action potentials in connected neurons induced a robust facilitation of
346 postsynaptic responses in both postsynaptic response rate and uEPSC amplitude under baseline
347 conditions (Figure 4B-D). Notably, the response rate to the first presynaptic action potential, which is
348 the number of presynaptic action potentials that generate a postsynaptic response, was low in non-
349 lesioned cultures (~3%; Figure 4C). In lesioned cultures, however, a significant increase in the synaptic

350 reliability for the first two pulses was observed. For the last three pulses in one train of stimulation,
351 averaged synaptic response rate levels became similar (Figure 4C). Moreover, the uEPSC amplitude
352 was significantly increased in response to the individual pulses 3 days after ECL (Figure 4D). The dGC-
353 to-CA3-PC paired recordings in the steady-state environment of organotypic tissue cultures therefore
354 provided evidence that synaptic transmission at hippocampal mossy fiber synapses is a target for lesion-
355 induced remodeling of hippocampal networks.

356 **Synaptopodin and the spine apparatus organelle are associated with dendritic ribosomes and**
357 **synapse-related mRNAs**

358 Hippocampal mossy fiber synapses show a complex organization of their pre- and postsynaptic sites.
359 Among these features, a regular occurrence of the spine apparatus organelle has been reported at the
360 postsynaptic site (Chicurel and Harris, 1992). Using transmission electron microscopy, a close
361 correlation between ribosomes and the spine apparatus organelle was readily revealed (Figure 5A).
362 Therefore, we quantified the presence of ribosomes in randomly selected dendritic spines that either
363 contain or lack the spine apparatus organelle at proximal apical dendritic segments in transmission
364 electron micrographs of the CA3 subfield (Figure 5B). We found that approx. 50% of dendritic spine
365 cross sections that lacked a spine apparatus contained ribosomes. When the spine apparatus organelle
366 was present in dendritic spine cross sections, however, approx. 90% contained ribosomes. To strengthen
367 the association between synaptopodin/the spine apparatus organelle and ribosomes, we performed
368 synaptopodin co-immunoprecipitation experiments of hippocampal lysates from adult animals followed
369 by negative contrast electron microscopy (Figure 5C). Here, we found ribosomes organized along
370 filamentous structures. Since these findings suggested an association between synaptopodin/the spine
371 apparatus organelle and ribosomes, which might contribute to plasticity-related local protein synthesis,
372 we performed a transcriptome analysis of Synpo-coIP enriched mRNA (Figure 5D, extended data table
373 5-1). After correction of unspecific antibody pull-downs by using synaptopodin-KO tissue lysates, a
374 considerable number of mRNAs was enriched after Synpo-coIP (violet dots; 1288 mRNAs).
375 Subsequently, a gene set enrichment analysis (g:Profiler) was performed to elucidate the functional
376 relevance of synaptopodin-associated mRNAs (Figure 5E). Among others, an enrichment in synapse-
377 related gene sets was identified. Therefore, these data indicate an association between synaptopodin/the
378 spine apparatus organelle and ribosomes, which might contribute to lesion-induced synaptic plasticity
379 through local protein synthesis.

380 **Ultrastructural reorganization of the spine apparatus organelle**

381 Previous studies have demonstrated that the ultrastructural organization of the spine apparatus organelle
382 might represent a target for plasticity (Vlachos et al., 2013; Lenz et al., 2021b). To study lesion-induced
383 effects on the ultrastructural organization of the spine apparatus organelle, we performed transmission
384 electron microscopy of mossy fiber synapses in non-lesioned and lesioned (3dp ECL) entorhino-

385 hippocampal tissue cultures (Figure 5F; c.f., (Vlachos et al., 2013)). No differences in the structural
386 organization of pre- and postsynaptic sites could be detected between the groups (presynapse: mossy
387 fiber perimeter: 11.61 ± 0.4 µm (control; n = 120) vs. 10.88 ± 0.35 µm (3dp ECL; n = 90); postsynapse:
388 number of PSDs: 4.91 ± 0.33 (control; n = 120) vs. 4.6 ± 0.27 (3dp ECL; n = 90), length of PSDs: 201
389 nm ± 4.35 (control; n = 589) vs. 201.7 ± 5.42 nm (3dp ECL; n = 414); values indicate mean ± sem,
390 Mann-Whitney test). Nevertheless, a substantial reorganization of the spine apparatus organelle was
391 evident in lesioned cultures 3 days after injury compared to non-lesioned controls (Figure 5G, H). We
392 found an increased number of dense plates in spine apparatus organelles from lesioned cultures (Figure
393 5G). At the same time the length of individual dense plates was significantly reduced in lesioned cultures
394 (Figure 5H). Therefore, we conclude that the spine apparatus organelle represents a target for lesion-
395 induced changes at hippocampal mossy fiber synapses.

396 **Synaptopodin-deficient tissue cultures show deficits in homeostatic synaptic plasticity upon**
397 **partial denervation**

398 Based on our ultrastructural analysis, we hypothesized that the spine apparatus organelle might
399 contribute to lesion-induced synaptic plasticity at hippocampal mossy fiber synapses. To gain further
400 insights concerning the role of the spine apparatus organelle, we performed experiments in
401 synaptopodin-deficient tissue preparations, which lack the spine apparatus organelle (Figure 6; (Deller
402 et al., 2003)).
403 Synaptopodin-deficient dGCs showed a significant increase in both the mean sEPSC amplitude and area
404 as well as the mean sEPSC half width 3 days following ECL (Figure 6A). In contrast, no changes in the
405 mean sEPSC frequency, which have been observed in wildtype (Synpo$^{+/+}$) cultures, were detected
406 (Figure 6B). Moreover, passive membrane properties remained stable upon lesion in synaptopodin-
407 deficient tissue preparations (Figure 6C).
408 In CA3-PCs, no significant changes in the sEPSC event analysis (Figure 6D) or the mean sEPSC
409 frequency (Figure 6E) were observed upon lesion. Again, passive membrane properties remained
410 unchanged (Figure 6F). Thus, our finding highlight altered lesion-induced synaptic adaptations for both
411 dGCs and CA3-PCs in synaptopodin-deficient tissue cultures.
412 We extended these findings with dGC-to-CA3-PC paired whole-cell patch-clamp recordings in
413 synaptopodin-deficient preparations (Figure 6G). In contrast to wildtype cultures, no significant
414 differences in the synaptic reliability could be detected 3 days after ECL (Figure 6H). We found a
415 significant reduction in the pulse-related uEPSC amplitude of successfully transmitted events in
416 lesioned synaptopodin-deficient preparations (Figure 6I). Notably, excitatory neurotransmission
417 seemed facilitated under baseline conditions as compared to wildtype cultures as indicated by significant
418 changes in sEPSC half width, area and amplitude/frequency-plots (Figure 7 A, B). Moreover, changes
419 in uEPSCs at mossy fiber synapses were evident in paired recordings (Figure 7 C, D). Hence,
420 synaptopodin-deficient mossy fiber synapses responded with a synaptic depression rather than

421 strengthening after the lesion. Taken together, these findings demonstrate the functional relevance for
422 the presence of synaptopodin in regulating lesion-induced plasticity at hippocampal mossy fiber
423 synapses.

424 **Entorhinal cortex lesion causes synaptopodin-dependent changes in the region-specific**
425 **hippocampal transcriptome**

426 To further explore synaptopodin-dependent changes in hippocampal subfields upon lesion, we
427 performed transcriptome analyses of both the DG and the CA3 region in non-lesion and lesioned
428 wildtype (Synpo$^{+/+}$) and synaptopodin-deficient (Synpo$^{-/-}$) cultures (Figure 8). The expression analysis
429 revealed a considerable number of genes that are differentially expressed in both hippocampal regions
430 from wildtype animals (Figure 8A, B). In contrast, synaptopodin-deficient tissue culture preparations
431 showed deficits in the lesion-induced adjustment of gene expression in the CA3 region (Figure 8A).
432 Moreover, wildtype and synaptopodin-deficient tissue preparations showed a genotype dependent gene
433 expression adjustment upon lesion in both regions although a common set of regulated genes was
434 identified (Figure 8B; for detailed tabular results see extended data tables 8-1, 8-2, 8-3, 8-4). We
435 therefore conclude that lesion-induced transcriptomic changes might depend on synaptopodin.
436 Unbiased gene set enrichment analysis for differentially expressed genes (gene ontology – molecular
437 function; GO:MF) from wildtype CA3 samples revealed that ECL caused changes in gene expression
438 related to ubiquitin- and GTP-related signaling (Figure 8C). Additionally, significant enrichments in
439 vesicle-, glia- and synapse-related gene sets were evident (gene ontology – cellular compartment;
440 GO:CC). In order to learn more about lesion-induced differential expression of synaptic gene sets in the
441 CA3 region ("synapse"; GOCC: 0045202), differentially expressed gene lists were filtered according to
442 the content of the respective gene ontology (Figure 8D). Here, 153 differentially expressed synaptic
443 genes were identified.
444 The same analyses were performed for wildtype DG samples (Figure 8E, F). In addition to changes in
445 ubiquitin- and GTP-related signaling genes, enrichments were seen for actin and transcription factor
446 binding (gene ontology – molecular function; GO:MF, Figure 8E). Moreover, endosome and
447 mitochondria related gene sets were enriched (gene ontology – cellular compartment; GO:CC). Again,
448 160 differentially expressed synaptic genes were identified in DG samples upon lesion (Figure 8F).
449 We conclude that the entorhinal cortex lesion caused regional transcriptome changes that might
450 contribute to the implementation of lesion-induced synaptic plasticity.

DISCUSSION

Denervation is a common phenomenon in numerous medical conditions affecting the central nervous system, which can trigger lesion-induced reorganization in neural networks (Vlachos et al., 2012c; Hengen et al., 2013; Lambo and Turrigiano, 2013; Platschek et al., 2016; Barnes et al., 2017; Bissen et al., 2021). In line with previous findings that employed proximity proteomics of synaptopodin (Falahati et al., 2022), we identified an association between synaptopodin and ribosomes. Using synaptopodin co-immunoprecipitation experiments, we report a synaptopodin-related transcriptome, which might contribute to lesion-induced plasticity. Together with findings that indicate interactions between synaptopodin, ribosomal subunits and ER-related proteins (Falahati et al., 2022), we suggest a role for synaptopodin as local regulator of synaptic plasticity.

To study lesion-induced changes in synaptic transmission, we used the *in vitro* model of ECL in organotypic entorhino-hippocampal tissue cultures. After *in vitro* maturation, tissue organization reaches a steady-state that is characterized by an *in vivo* like ultrastructural synaptic architecture (Haber et al., 2006; Heller and Rusakov, 2017). In this context, recent work has demonstrated that organotypic hippocampal tissue cultures have intact mossy fiber pathways and synapses (Maus et al., 2020). Moreover, the excitatory cortical input – the perforant path – terminates at distal apical dendrites of dGCs and pyramidal neurons of the ammonic subregions (Frotscher and Heimrich, 1995; Frotscher et al., 1995; Frotscher et al., 1997; Lenz et al., 2023). Our results demonstrate lesion-induced excitatory synaptic strengthening in both dGCs and CA3-PCs upon lesion, which is accompanied by changes in the region-specific transcriptome. Moreover, we here used paired whole-cell patch-clamp recordings to assess synaptic transmission at individual hippocampal mossy fiber synapses – the monosynaptic excitatory contacts between dGCs and CA3-PCs – in a steady-state environment. In this experimental approach, we identified denervation-induced adaptations at hippocampal mossy fiber synapses. In addition, ultrastructural changes in the volume of synapses as well as in the spine apparatus organelle, which is well established in the regulation of synaptic plasticity (Vlachos et al., 2013; Lenz et al., 2021b), were observed after ECL. Since adaptations on both synaptic and transcriptomic levels were altered in synaptopodin-deficient tissue cultures, we assert a crucial regulatory role for synaptopodin and the spine apparatus organelle in orchestrating lesion-induced plasticity.

Lesion-induced excitatory synaptic strengthening might aim at compensating for the loss of input. The compensatory adjustment of excitatory synaptic strength, which aims at re-achieving distinct physiological setpoints in neural networks, has been summarized as homeostatic synaptic plasticity (Mahoney et al., 2014). In this study, we did not observe changes in dGC firing rates upon lesion that might be restored by synaptic adaptations in a homeostatic fashion. However, the stability and adjustment of excitatory neurotransmission after lesion suggest the recruitment of homeostatic mechanisms. Since our 3D reconstruction of synapses revealed the rapid implementation of changes in synapse structure and complexity, it is intriguing to theorize that compensatory plasticity at remaining

487 intra-hippocampal pathways might operate on different time scales to rapidly stabilize neuronal function
488 upon denervation.
489 The dentate gyrus/CA3 neural network is an integral component of the trisynaptic hippocampal
490 pathway. The hippocampal mossy fiber pathway forms large *en passant* synapses and connects one
491 individual dGC to a limited number of CA3-PCs (Acsady et al., 1998). Both regions receive cortical
492 input – the perforant path – from entorhinal layer II stellate cells that can induce, promote and modulate
493 information processing in hippocampal subregions. Moreover, this pathway is known to be implicated
494 various diseases; among them traumatic, inflammatory and neurodegenerative conditions like
495 Alzheimer's disease (AD; (Thal et al., 2000; Robinson et al., 2014)). Additionally, the hippocampal
496 mossy fiber synapse has been linked to memory acquisition and retrieval (Marr, 1971; Hunsaker et al.,
497 2008). Specifically, activity-dependent structural and functional changes in synaptic features can encode
498 input patterns for a prolonged period of time (Lee et al., 2013; Vandael et al., 2020). Again, alterations
499 in hippocampal mossy fiber transmission have been reported in animal models of Alzheimer's disease
500 (AD) and aging related cognitive decline (Villanueva-Castillo et al., 2017; Viana da Silva et al., 2019).
501 Nevertheless, it remains unclear if the lesion-induced synaptic response deteriorates cognitive
502 performance by affecting information processing in neural networks.
503 Recently, characteristic features of transmission and stabilizing factors at hippocampal mossy fiber
504 synapses have been revealed (Vyleta and Jonas, 2014; Vyleta et al., 2016; De Bruyckere et al., 2018;
505 Vandael et al., 2021a). Upon presynaptic activity, a detonating behavior can be observed, in which a
506 limited number of – but not single – action potentials can elicit a suprathreshold postsynaptic
507 depolarization (Henze et al., 2002a). Although this phenomenon has been extensively described in
508 mossy fiber bouton-CA3-PC paired recordings (Vandael et al., 2021b), we were not able to reveal
509 detonating characteristics in dGC-CA3-PC pairs. Here, differences in the experimental model and
510 methodology can account for the divergent observation of detonator characteristics. In line with
511 previous reports, however, a filtering of single action potentials with a subsequent robust facilitation of
512 synaptic transmission at this synapse was evident (Zalutsky and Nicoll, 1990; Gundlfinger et al., 2007).
513 Our results demonstrate that the partial loss of input following lesion can influence both synaptic
514 reliability and potency, which has been observed for other plasticity-inducing stimuli at this synapse
515 (Zalutsky and Nicoll, 1990). We suggest that lesion-induced modulation of filtering/facilitation
516 properties might interact with network phenomena, such as pattern separation and completion along the
517 dentate gyrus/CA3-axis (O'Reilly and McClelland, 1994; Leutgeb et al., 2007; Prince et al., 2016).
518 Moreover, the presence of synaptopodin may interfere with this network process under baseline and
519 plasticity-inducing conditions accounting for the previously reported cognitive deficits in synaptopodin-
520 deficient mice (Deller et al., 2003) and the synaptopodin-related cognitive decline during human aging
521 (Wingo et al., 2019).
522 Of note, it is an established view that mossy fiber synaptic plasticity is predominantly mediated by
523 presynaptic processes (Vandael et al., 2020; Orlando et al., 2021; Monday et al., 2022). Nevertheless,

524 recent work has suggested that the postsynaptic site shapes the transmission and plasticity through
525 transsynaptic mechanisms (Vandael et al., 2021a). In this study, we report that the spine apparatus
526 organelle regulates denervation-induced synaptic plasticity at this synapse. Since its discovery, the
527 function of the spine apparatus organelle and the mechanisms through which it orchestrates synaptic
528 plasticity remained enigmatic. By using electron microscopy and co-immunprecipitation experiments,
529 we here demonstrated that synaptopodin and the spine apparatus organelle are associated with
530 ribosomes. However, it remains unclear if these are direct or indirect interactions and co-
531 immunoprecipitation might target mRNA transport/storage granules. Given the lesion-induced
532 ultrastructural remodeling of the spine apparatus organelle, it is interesting to speculate whether these
533 changes might orchestrate the previously reported local protein synthesis in close proximity to
534 synaptopodin clusters (Vlachos et al., 2009; Dubes et al., 2022). Since (1) lesion-induced synaptic
535 plasticity is altered in synaptopodin-deficient tissue preparations and (2) alterations in synaptopodin
536 expression have been linked to cognitive decline (Wingo et al., 2019), we hypothesize that
537 synaptopodin-dependent plasticity might stabilize cognitive performance by increasing synaptic
538 resilience (Yap et al., 2020).

ACKNOWLEDGEMENTS

The Galaxy server that was used for some calculations in this study is partially funded by Collaborative Research Centre 992 Medical Epigenetics (DFG grant SFB 992/1 2012) and German Federal Ministry of Education and Research (BMBF grants 031 A538A/A538C RBC, 031L0101B/031L0101C de.NBI-epi, and 031L0106 de.STAIR (de.NBI)). We thank Bernd Heimrich and Amelie Eichler for helpful and stimulating discussions on ultrastructural mossy fiber architecture. We thank Susanne Faßbender and Sigrun Nestel for excellent technical assistance in electron microscopy. Moreover, we thank Robert Lindner for insightful discussions on synaptopodin co-immunoprecipitations. This work was supported by Else Kröner-Fresenius-Stiftung (EKFS_#2019_A94 to ML) and Deutsche Forschungsgemeinschaft (DFG; Project-ID 259373024 B14–CRC/TRR 167 to AV).

REFERENCES

Acsady L, Kamondi A, Sik A, Freund T, Buzsaki G (1998) GABAergic cells are the major postsynaptic targets of mossy fibers in the rat hippocampus. J Neurosci 18:3386-3403.

Afgan E, Baker D, Batut B, van den Beek M, Bouvier D, Cech M, Chilton J, Clements D, Coraor N, Gruning BA, Guerler A, Hillman-Jackson J, Hiltemann S, Jalili V, Rasche H, Soranzo N, Goecks J, Taylor J, Nekrutenko A, Blankenberg D (2018) The Galaxy platform for accessible, reproducible and collaborative biomedical analyses: 2018 update. Nucleic Acids Res 46:W537-W544.

Barnes SJ, Franzoni E, Jacobsen RI, Erdelyi F, Szabo G, Clopath C, Keller GB, Keck T (2017) Deprivation-Induced Homeostatic Spine Scaling In Vivo Is Localized to Dendritic Branches that Have Undergone Recent Spine Loss. Neuron 96:871-882 e875.

Batut B, van den Beek M, Doyle MA, Soranzo N (2021) RNA-Seq Data Analysis in Galaxy. Methods Mol Biol 2284:367-392.

Beike L, Wrede C, Hegermann J, Lopez-Rodriguez E, Kloth C, Gauldie J, Kolb M, Maus UA, Ochs M, Knudsen L (2019) Surfactant dysfunction and alveolar collapse are linked with fibrotic septal wall remodeling in the TGF-beta1-induced mouse model of pulmonary fibrosis. Lab Invest 99:830-852.

Bissen D, Kracht MK, Foss F, Hofmann J, Acker-Palmer A (2021) EphrinB2 and GRIP1 stabilize mushroom spines during denervation-induced homeostatic plasticity. Cell Rep 34:108923.

Cardona A, Saalfeld S, Schindelin J, Arganda-Carreras I, Preibisch S, Longair M, Tomancak P, Hartenstein V, Douglas RJ (2012) TrakEM2 software for neural circuit reconstruction. PLoS One 7:e38011.

Chicurel ME, Harris KM (1992) Three-dimensional analysis of the structure and composition of CA3 branched dendritic spines and their synaptic relationships with mossy fiber boutons in the rat hippocampus. J Comp Neurol 325:169-182.

De Bruyckere E, Simon R, Nestel S, Heimrich B, Katzel D, Egorov AV, Liu P, Jenkins NA, Copeland NG, Schwegler H, Draguhn A, Britsch S (2018) Stability and Function of Hippocampal Mossy Fiber Synapses Depend on Bcl11b/Ctip2. Front Mol Neurosci 11:103.

Del Turco D, Deller T (2007) Organotypic entorhino-hippocampal slice cultures--a tool to study the molecular and cellular regulation of axonal regeneration and collateral sprouting in vitro. Methods Mol Biol 399:55-66.

Deller T, Korte M, Chabanis S, Drakew A, Schwegler H, Stefani GG, Zuniga A, Schwarz K, Bonhoeffer T, Zeller R, Frotscher M, Mundel P (2003) Synaptopodin-deficient mice lack a spine apparatus and show deficits in synaptic plasticity. Proc Natl Acad Sci U S A 100:10494-10499.

Dubes S, Soula A, Benquet S, Tessier B, Poujol C, Favereaux A, Thoumine O, Letellier M (2022) miR-124-dependent tagging of synapses by synaptopodin enables input-specific homeostatic plasticity. EMBO J:e109012.

Falahati H, Wu Y, Feuerer V, Simon HG, De Camilli P (2022) Proximity proteomics of synaptopodin provides insight into the molecular composition of the spine apparatus of dendritic spines. Proc Natl Acad Sci U S A 119:e2203750119.

Frotscher M, Heimrich B (1995) Lamina-specific synaptic connections of hippocampal neurons in vitro. J Neurobiol 26:350-359.

Frotscher M, Heimrich B, Deller T (1997) Sprouting in the hippocampus is layer-specific. Trends Neurosci 20:218-223.

Frotscher M, Heimrich B, Deller T, Nitsch R (1995) Understanding the cortex through the hippocampus: lamina-specific connections of the rat hippocampal neurons. J Anat 187 (Pt 3):539-545.

Galaxy C (2022) The Galaxy platform for accessible, reproducible and collaborative biomedical analyses: 2022 update. Nucleic Acids Res.

Goecks J, Nekrutenko A, Taylor J, Galaxy T (2010) Galaxy: a comprehensive approach for supporting accessible, reproducible, and transparent computational research in the life sciences. Genome Biol 11:R86.

Gundlfinger A, Leibold C, Gebert K, Moisel M, Schmitz D, Kempter R (2007) Differential modulation of short-term synaptic dynamics by long-term potentiation at mouse hippocampal mossy fibre synapses. J Physiol 585:853-865.

Haber M, Zhou L, Murai KK (2006) Cooperative astrocyte and dendritic spine dynamics at hippocampal excitatory synapses. J Neurosci 26:8881-8891.

Heller JP, Rusakov DA (2017) The Nanoworld of the Tripartite Synapse: Insights from Super-Resolution Microscopy. Front Cell Neurosci 11:374.

Hengen KB, Lambo ME, Van Hooser SD, Katz DB, Turrigiano GG (2013) Firing rate homeostasis in visual cortex of freely behaving rodents. Neuron 80:335-342.

Henze DA, Wittner L, Buzsaki G (2002a) Single granule cells reliably discharge targets in the hippocampal CA3 network in vivo. Nat Neurosci 5:790-795.

Henze DA, McMahon DB, Harris KM, Barrionuevo G (2002b) Giant miniature EPSCs at the hippocampal mossy fiber to CA3 pyramidal cell synapse are monoquantal. J Neurophysiol 87:15-29.

Hunsaker MR, Rosenberg JS, Kesner RP (2008) The role of the dentate gyrus, CA3a,b, and CA3c for detecting spatial and environmental novelty. Hippocampus 18:1064-1073.

Jedlicka P, Deller T (2017) Understanding the role of synaptopodin and the spine apparatus in Hebbian synaptic plasticity - New perspectives and the need for computational modeling. Neurobiol Learn Mem 138:21-30.

Jedlicka P, Schwarzacher SW, Winkels R, Kienzler F, Frotscher M, Bramham CR, Schultz C, Bas Orth C, Deller T (2009) Impairment of in vivo theta-burst long-term potentiation and network excitability in the dentate gyrus of synaptopodin-deficient mice lacking the spine apparatus and the cisternal organelle. Hippocampus 19:130-140.

Korkotian E, Frotscher M, Segal M (2014) Synaptopodin regulates spine plasticity: mediation by calcium stores. J Neurosci 34:11641-11651.

Lambo ME, Turrigiano GG (2013) Synaptic and intrinsic homeostatic mechanisms cooperate to increase L2/3 pyramidal neuron excitability during a late phase of critical period plasticity. J Neurosci 33:8810-8819.

Lee KJ, Queenan BN, Rozeboom AM, Bellmore R, Lim ST, Vicini S, Pak DT (2013) Mossy fiber-CA3 synapses mediate homeostatic plasticity in mature hippocampal neurons. Neuron 77:99-114.
Lenz M, Galanis C, Kleidonas D, Fellenz M, Deller T, Vlachos A (2019) Denervated mouse dentate granule cells adjust their excitatory but not inhibitory synapses following in vitro entorhinal cortex lesion. Exp Neurol 312:1-9.
Lenz M, Eichler A, Kruse P, Muellerleile J, Deller T, Jedlicka P, Vlachos A (2021a) All-trans retinoic acid induces synaptopodin-dependent metaplasticity in mouse dentate granule cells. Elife 10.
Lenz M, Kruse P, Eichler A, Straehle J, Beck J, Deller T, Vlachos A (2021b) All-trans retinoic acid induces synaptic plasticity in human cortical neurons. Elife 10.
Lenz M, Eichler A, Kruse P, Galanis C, Kleidonas D, Andrieux G, Boerries M, Jedlicka P, Muller U, Deller T, Vlachos A (2023) The Amyloid Precursor Protein Regulates Synaptic Transmission at Medial Perforant Path Synapses. J Neurosci 43:5290-5304.
Leutgeb JK, Leutgeb S, Moser MB, Moser EI (2007) Pattern separation in the dentate gyrus and CA3 of the hippocampus. Science 315:961-966.
Lipp HP, Schwegler H, Heimrich B, Driscoll P (1988) Infrapyramidal mossy fibers and two-way avoidance learning: developmental modification of hippocampal circuitry and adult behavior of rats and mice. J Neurosci 8:1905-1921.
Maggio N, Vlachos A (2018) Tumor necrosis factor (TNF) modulates synaptic plasticity in a concentration-dependent manner through intracellular calcium stores. J Mol Med (Berl) 96:1039-1047.
Mahoney RE, Rawson JM, Eaton BA (2014) An age-dependent change in the set point of synaptic homeostasis. J Neurosci 34:2111-2119.
Marr D (1971) Simple memory: a theory for archicortex. Philos Trans R Soc Lond B Biol Sci 262:23-81.
Maus L, Lee C, Altas B, Sertel SM, Weyand K, Rizzoli SO, Rhee J, Brose N, Imig C, Cooper BH (2020) Ultrastructural Correlates of Presynaptic Functional Heterogeneity in Hippocampal Synapses. Cell Rep 30:3632-3643 e3638.
Mesulam MM, Lalehzari N, Rahmani F, Ohm D, Shahidehpour R, Kim G, Gefen T, Weintraub S, Bigio E, Geula C (2019) Cortical cholinergic denervation in primary progressive aphasia with Alzheimer pathology. Neurology 92:e1580-e1588.
Monday HR, Kharod SC, Yoon YJ, Singer RH, Castillo PE (2022) Presynaptic FMRP and local protein synthesis support structural and functional plasticity of glutamatergic axon terminals. Neuron 110:2588-2606 e2586.
O'Reilly RC, McClelland JL (1994) Hippocampal conjunctive encoding, storage, and recall: avoiding a trade-off. Hippocampus 4:661-682.
Orlando M, Dvorzhak A, Bruentgens F, Maglione M, Rost BR, Sigrist SJ, Breustedt J, Schmitz D (2021) Recruitment of release sites underlies chemical presynaptic potentiation at hippocampal mossy fiber boutons. PLoS Biol 19:e3001149.
Platschek S, Cuntz H, Vuksic M, Deller T, Jedlicka P (2016) A general homeostatic principle following lesion induced dendritic remodeling. Acta Neuropathol Commun 4:19.
Prang P, Del Turco D, Deller T (2003) Associational sprouting in the mouse fascia dentata after entorhinal lesion in vitro. Brain Res 978:205-212.
Prince LY, Bacon TJ, Tigaret CM, Mellor JR (2016) Neuromodulation of the Feedforward Dentate Gyrus-CA3 Microcircuit. Front Synaptic Neurosci 8:32.
Raudvere U, Kolberg L, Kuzmin I, Arak T, Adler P, Peterson H, Vilo J (2019) g:Profiler: a web server for functional enrichment analysis and conversions of gene lists (2019 update). Nucleic Acids Res 47:W191-W198.
Reimand J, Isserlin R, Voisin V, Kucera M, Tannus-Lopes C, Rostamianfar A, Wadi L, Meyer M, Wong J, Xu C, Merico D, Bader GD (2019) Pathway enrichment analysis and visualization of omics data using g:Profiler, GSEA, Cytoscape and EnrichmentMap. Nat Protoc 14:482-517.
Riegle KC, Meyer RL (2007) Rapid homeostatic plasticity in the intact adult visual system. J Neurosci 27:10556-10567.
Robinson JL, Molina-Porcel L, Corrada MM, Raible K, Lee EB, Lee VM, Kawas CH, Trojanowski JQ (2014) Perforant path synaptic loss correlates with cognitive impairment and Alzheimer's disease in the oldest-old. Brain 137:2578-2587.
Strehl A, Galanis C, Radic T, Schwarzacher SW, Deller T, Vlachos A (2018) Dopamine Modulates Homeostatic Excitatory Synaptic Plasticity of Immature Dentate Granule Cells in Entorhino-Hippocampal Slice Cultures. Front Mol Neurosci 11:303.
Sutton MA, Ito HT, Cressy P, Kempf C, Woo JC, Schuman EM (2006) Miniature neurotransmission stabilizes synaptic function via tonic suppression of local dendritic protein synthesis. Cell 125:785-799.
Tani H, Dulla CG, Farzampour Z, Taylor-Weiner A, Huguenard JR, Reimer RJ (2014) A local glutamate-glutamine cycle sustains synaptic excitatory transmitter release. Neuron 81:888-900.
Thal DR, Holzer M, Rub U, Waldmann G, Gunzel S, Zedlick D, Schober R (2000) Alzheimer-related tau-pathology in the perforant path target zone and in the hippocampal stratum oriens and radiatum correlates with onset and degree of dementia. Exp Neurol 163:98-110.
Turrigiano GG, Leslie KR, Desai NS, Rutherford LC, Nelson SB (1998) Activity-dependent scaling of quantal amplitude in neocortical neurons. Nature 391:892-896.
Vandael D, Okamoto Y, Jonas P (2021a) Transsynaptic modulation of presynaptic short-term plasticity in hippocampal mossy fiber synapses. Nat Commun 12:2912.
Vandael D, Borges-Merjane C, Zhang X, Jonas P (2020) Short-Term Plasticity at Hippocampal Mossy Fiber Synapses Is Induced by Natural Activity Patterns and Associated with Vesicle Pool Engram Formation. Neuron 107:509-521 e507.
Vandael D, Okamoto Y, Borges-Merjane C, Vargas-Barroso V, Suter BA, Jonas P (2021b) Subcellular patch-clamp techniques for single-bouton stimulation and simultaneous pre- and postsynaptic recording at cortical synapses. Nat Protoc 16:2947-2967.

681 Viana da Silva S, Zhang P, Haberl MG, Labrousse V, Grosjean N, Blanchet C, Frick A, Mulle C (2019) Hippocampal Mossy
682 Fibers Synapses in CA3 Pyramidal Cells Are Altered at an Early Stage in a Mouse Model of Alzheimer's Disease. J
683 Neurosci 39:4193-4205.
684 Villanueva-Castillo C, Tecuatl C, Herrera-Lopez G, Galvan EJ (2017) Aging-related impairments of hippocampal mossy
685 fibers synapses on CA3 pyramidal cells. Neurobiol Aging 49:119-137.
686 Vlachos A, Bas Orth C, Schneider G, Deller T (2012a) Time-lapse imaging of granule cells in mouse entorhino-hippocampal
687 slice cultures reveals changes in spine stability after entorhinal denervation. J Comp Neurol 520:1891-1902.
688 Vlachos A, Korkotian E, Schonfeld E, Copanaki E, Deller T, Segal M (2009) Synaptopodin regulates plasticity of dendritic
689 spines in hippocampal neurons. J Neurosci 29:1017-1033.
690 Vlachos A, Muller-Dahlhaus F, Rosskopp J, Lenz M, Ziemann U, Deller T (2012b) Repetitive magnetic stimulation induces
691 functional and structural plasticity of excitatory postsynapses in mouse organotypic hippocampal slice cultures. J
692 Neurosci 32:17514-17523.
693 Vlachos A, Becker D, Jedlicka P, Winkels R, Roeper J, Deller T (2012c) Entorhinal denervation induces homeostatic
694 synaptic scaling of excitatory postsynapses of dentate granule cells in mouse organotypic slice cultures. PLoS One
695 7:e32883.
696 Vlachos A, Ikenberg B, Lenz M, Becker D, Reifenberg K, Bas-Orth C, Deller T (2013) Synaptopodin regulates denervation-
697 induced homeostatic synaptic plasticity. Proc Natl Acad Sci U S A 110:8242-8247.
698 Vyleta NP, Jonas P (2014) Loose coupling between Ca2+ channels and release sensors at a plastic hippocampal synapse.
699 Science 343:665-670.
700 Vyleta NP, Borges-Merjane C, Jonas P (2016) Plasticity-dependent, full detonation at hippocampal mossy fiber-CA3
701 pyramidal neuron synapses. Elife 5.
702 Weng FJ, Garcia RI, Lutzu S, Alvina K, Zhang Y, Dushko M, Ku T, Zemoura K, Rich D, Garcia-Dominguez D, Hung M,
703 Yelhekar TD, Sorensen AT, Xu W, Chung K, Castillo PE, Lin Y (2018) Npas4 Is a Critical Regulator of Learning-
704 Induced Plasticity at Mossy Fiber-CA3 Synapses during Contextual Memory Formation. Neuron 97:1137-1152
705 e1135.
706 Wingo AP, Dammer EB, Breen MS, Logsdon BA, Duong DM, Troncosco JC, Thambisetty M, Beach TG, Serrano GE,
707 Reiman EM, Caselli RJ, Lah JJ, Seyfried NT, Levey AI, Wingo TS (2019) Large-scale proteomic analysis of
708 human brain identifies proteins associated with cognitive trajectory in advanced age. Nat Commun 10:1619.
709 Yap K, Drakew A, Smilovic D, Rietsche M, Paul MH, Vuksic M, Del Turco D, Deller T (2020) The actin-modulating
710 protein synaptopodin mediates long-term survival of dendritic spines. Elife 9.
711 Zalutsky RA, Nicoll RA (1990) Comparison of two forms of long-term potentiation in single hippocampal neurons. Science
712 248:1619-1624.
713

714 **FIGURES**

715 **Figure 1: Entorhinal cortex lesion caused synaptic strengthening in both dGCs and CA3-PCs.**

716 (A) Entorhinal cortex lesion (ECL) in organotypic entorhino-hippocampal tissue cultures was
717 performed by dissecting the perforant path (white line, scale bar 300 µm). Cytoarchitecture was
718 visualized by DAPI nuclear staining.

719 (B) Spontaneous excitatory postsynaptic currents (sEPSCs) were recorded in both dGCs and CA3-PCs
720 in non-lesioned and lesioned cultures (3 days post lesion, 3 dp ECL).

721 (C-D) Spontaneous EPSC analysis in dGCs revealed a lesion-induced excitatory synaptic strengthening
722 in the mean sEPSC amplitude, half width and area (C; $n_{control}$ = 22 cells; $n_{3dp\ ECL}$ = 22 cells; Mann-
723 Whitney test; Linear regression fit for XY-plot analysis). Percentile analysis of sEPSC amplitudes (D)
724 demonstrated that the excitatory synaptic strengthening was evident in the 50% largest events (Mann-
725 Whitney test).

726 (E-F) The frequency of sEPSCs was significantly increased 3 days after ECL (E; Mann-Whitney test).
727 Moreover, amplitude/frequency-analysis shows that the abundance of larger sEPSC amplitudes was
728 higher in lesioned cultures when compared to non-lesioned controls (F; RM-two-way ANOVA followed
729 by Sidak's multiple comparisons test).

730 (G-H) Spontaneous EPSC analysis in CA3-PCs revealed a lesion-induced increase in mean sEPSC
731 amplitude, whereas half width and area remained unchanged (G; $n_{control}$ = 48 cells; $n_{3dp\ ECL}$ = 49 cells;
732 Mann-Whitney test; Linear regression fit for XY-plot analysis). Percentile analysis of sEPSC
733 amplitudes (H) demonstrated that the excitatory synaptic strengthening was only visible in the 50%
734 largest events (Mann-Whitney test).

735 (I-J) No lesion-induced changes in mean sEPSC frequency were detectable in CA3-PCs.
736 Amplitude/frequency-analysis showed a reduced number of small events in CA3-PCs 3 days after ECL
737 (Mann-Whitney test for column statistics and RM-two-way ANOVA followed by Sidak's multiple
738 comparisons test for XY-plot analysis).

739 Individual data points are indicated by colored dots. Values represent mean ± s.e.m (*$p < 0.05$, **$p <$
740 0.01, ***$p < 0.001$, ns - non significant difference).

741 **Figure 2: Entorhinal cortex lesion did not influence active or passive membrane properties.**
742 (A-B) Sample traces of dGCs (A) and CA3-PCs (B) in current clamp mode at a current injection of -
743 100 pA (lower trace) and +300 pA (upper trace) in control cultures and 3 days post ECL.
744 (C, E) Both resting membrane potential and input resistance (C) as well as the input-output curve for
745 the first 15 sweeps of current injection (E) in dGCs were unaffected by ECL ($n_{control}$ = 22 cells; $n_{3dp\ ECL}$
746 = 22 cells; Mann-Whitney test and RM two-way ANOVA followed by Sidak's multiple comparisons
747 test for XY-plot analysis).
748 (E) Action potential frequency upon increasing current injection in dGCswas similar in non-lesioned
749 and lesioned cultures (RM two-way ANOVA followed by Sidak's multiple comparisons test).
750 (D, F) Both resting membrane potential and input resistance (D) as well as the input-output curve for
751 the first 15 sweeps of current injection (F) in CA3-PCs were unaffected by the ECL ($n_{control}$ = 48 cells;
752 $n_{3dp\ ECL}$ = 49 cells; Mann-Whitney test and RM two-way ANOVA followed by Sidak's multiple
753 comparisons test for XY-plot analysis).
754 (F) Action potential frequency upon increasing current injection in CA3-PCs is similar in non-lesioned
755 and lesioned cultures (RM two-way ANOVA followed by Sidak's multiple comparisons test).

756 Individual data points are indicated by colored dots. Values represent mean ± s.e.m (ns - non significant
757 difference).

Figure 3: Entorhinal cortex lesion induced ultrastructural synaptic changes in DG and CA3 subfields.

(A) 3D-reconstructions of synapses (based on SBF-SEM) onto proximal and distal apical dendrites in the dentate gyrus (postsynaptic compartment, green; presynaptic compartment, red).

(B) Analysis of both post- and presynaptic volumes from 3D-reconstructions in proximal DG areas. A decrease in postsynaptic volume was detected after lesion while presynaptic volume remained stable (postsynaptic compartments: $n_{control}$ = 170 postsynapses, $n_{2hp\ ECL}$ = 286 postsynapses, $n_{3dp\ ECL}$ = 223 postsynapses; presynaptic compartments: $n_{control}$ = 163 presynapses, $n_{2hp\ ECL}$ = 243 presynapses, $n_{3dp\ ECL}$ = 158 presynapses from one representative tissue culture each; Kruskal-Wallis test followed by Dunn's post-hoc correction).

(C) Analysis of synaptic complexity, which is the number of postsynaptic sites per presynaptic bouton, at proximal synapses in DG. Notably, synaptic complexity increases following entorhinal cortex lesion.

(D) Analysis of both post- and presynaptic volumes in distal DG areas. A decrease in postsynaptic and presynaptic volumes were detected (postsynaptic compartments: $n_{control}$ = 54 postsynapses, $n_{2hp\ ECL}$ = 82 postsynapses, $n_{3dp\ ECL}$ = 48 postsynapses; presynaptic compartments: $n_{control}$ = 49 presynapses, $n_{2hp\ ECL}$ = 74 presynapses, $n_{3dp\ ECL}$ = 38 presynapses from one representative tissue culture each; Kruskal-Wallis test followed by Dunn's post-hoc correction).

(E) Synaptic complexity at distal synapses in DG remained unchanged following lesion.

(F) 3D-reconstructions of synapses (based on SBF-SEM) onto proximal and distal apical dendrites in the CA3 region (postsynaptic compartment, green; presynaptic compartment, red).

(G) Analysis of both post- and presynaptic volumes in proximal CA3 areas. An increase in presynaptic volume was detected while postsynaptic volumes remained unchanged (postsynaptic compartments: $n_{control}$ = 208 postsynapses, $n_{2hp\ ECL}$ = 224 postsynapses, $n_{3dp\ ECL}$ = 219 postsynapses; presynaptic compartments: $n_{control}$ = 159 presynapses, $n_{2hp\ ECL}$ = 202 presynapses, $n_{3dp\ ECL}$ = 168 presynapses from one representative tissue culture each; Kruskal-Wallis test followed by Dunn's post-hoc correction).

(H) Synaptic complexity at proximal synapses in CA3 remained widely unchanged following lesion.

(I) Analysis of both post- and presynaptic volumes in distal CA3 areas. A decrease in postsynaptic volume was evident while presynaptic volumes remained unchanged (postsynaptic compartments: $n_{control}$ = 99 postsynapses, $n_{2hp\ ECL}$ = 120 postsynapses, $n_{3dp\ ECL}$ = 120 postsynapses; presynaptic compartments: $n_{control}$ = 77 presynapses, $n_{2hp\ ECL}$ = 98 presynapses, $n_{3dp\ ECL}$ = 93 presynapses from one representative tissue culture each; Kruskal-Wallis test followed by Dunn's post-hoc correction).

(J) Despite a trend towards reduced complexity, distal synapses in CA3 remained widely unchanged following entorhinal cortex lesion.

Graphs depict box plots (box: 25-75 percentile; whiskers: 10-90 percentile; line indicates median), values outside this range were indicated by individual dots (*$p < 0.05$, **$p < 0.01$, ***$p < 0.001$, ns - non significant difference).

794 **Figure 4: Lesion-induced loss of the cortico-hippocampal projection changed transmission at**
795 **hippocampal mossy fiber synapses.**
796 (A) Post-hoc visualization of patched neurons in organotypic tissue cultures after paired-
797 electrophysiological recordings between individual presynaptic (pre) GCs of the dentate gyrus (DG)
798 and postsynaptic (post) CA3-PCs to analyze synaptic transmission features at hippocampal mossy fiber
799 synapses (scale bar 300 µm).
800 (B) Five consecutive action potentials were induced in dGCs at 20 Hz (bottom trace) to assess
801 postsynaptic responses in CA3-PCs in lesioned and non-lesioned cultures (upper traces).
802 (C) The response rate, i.e., the fraction of presynaptic pulses that elicited a postsynaptic response in a
803 connected pair of individual neurons, was significantly increased for the first two pulses in lesioned
804 cultures when compared to non-lesioned controls ($n_{control}$ = 10; $n_{3dp\ ECL}$ = 10; Mann-Whitney test for the
805 respective pulse numbers).
806 (D) In successfully elicited unitary EPSCs (uEPSCs), a significant increase in uEPSC amplitude was
807 detectable ($n°1_{control}$ = 20 events, $n°1_{ECL}$ = 187 events; $n°2_{control}$ = 115 events, $n°2_{ECL}$ = 304 events;
808 $n°3_{control}$ = 292 events, $n°3_{ECL}$ = 394 events (one data point outside the axis limits); $n°4_{control}$ = 326 events,
809 $n°4_{ECL}$ = 385 events; $n°5_{control}$ = 307 events, $n°5_{ECL}$ = 384 events; Mann-Whitney test for the respective
810 pulse numbers).

811 Individual data points are indicated by colored dots. Values represent mean ± s.e.m (*$p < 0.05$, **$p <$
812 0.01, ***$p < 0.001$, ns - non significant difference).

Figure 5: The spine apparatus organelle assembled ribosomes and excitatory synapse related mRNAs.

(A) Transmission electron microscopy (TEM) images demonstrate a close association of ribosomes (arrowheads) and the spine apparatus organelle. Scale bar upper image 300 nm, scale bar lower image 400 nm.

(B) Assessment of ribosomes in cross sections of dendritic spines depending on the presence of the spine apparatus organelle (SA). In spine cross sections lacking a spine apparatus organelle, approx. 50% of spines contained ribosomes. Notably, approx. 90% of the spines containing the spine apparatus organelle also contained ribosomes.

(C) Negative contrast electron microscopy images from beads used from synaptopodin co-immunoprecipitation in hippocampal tissue from adult animals. Micrographs illustrate the immunoprecipitation of ribosomes and ribosomal subunits (white non-contrasted areas), which are organized along microfilaments suggesting an association between synaptopodin and ribosomes. Scale bars 100 nm.

(D) Analysis of differential mRNA abundance in Synpo-coIP RNA samples compared to their respective input samples to reveal the synaptopodin related transcriptome (extended data table 5-1). A log2(FC) value > 0 indicates an mRNA enrichment in Synpo-coIP samples. To rule out the unspecific pull-down of targets, the same experimental protocol was applied to synaptopodin KO tissue lysates. Log2(FC) values were plotted for differentially enriched genes ($p_{adj.} < 0.05$) from wildtype tissue cultures and specific enrichment was assumed if FC increased more than 30% (violet dots, wildtype: n = 5 samples and Synpo-KO: n = 2 samples input and Synpo-coIP respectively; 5-6 tissue cultures pooled from one filter per sample; DESeq2-analysis).

(E) A gene set enrichment analysis for a cellular compartment gene ontology was performed for significantly enriched genes in Synpo-coIP samples and visualized by the g:Profiler web application. Notably, synaptic gene sets were enriched.

(F) Transmission electron microscopy was used to visualize ultrastructural properties of mossy fiber synapses in lesioned and non-lesioned control cultures (scale bar, 1 µm). Spine apparatus organelle are marked by white arrowheads.

(G) Upon lesion, the abundance of spine apparatus organelles (SA) and their number of dense plates were significantly increased in the postsynaptic compartment of mossy fiber synapses ($n_{control}$ = 120 (no SA = 97 postsynapses, 1 dense plate = 22 postsynapses, 2 dense plates = 1 postsynapse, 3 dense plates = 0 postsynapses); n_{ECL} = 90 (no SA = 56 postsynapses, 1 dense plate = 21 postsynapses, 2 dense plates = 12 postsynapses, 3 dense plates = 1 postsynapses)).

(H) The length of the respective dense plates significantly decreased 3 days after ECL ($n_{control}$ = 24, one data point outside the axis limits; n_{ECL} = 48; Mann-Whitney test).

Individual data points are indicated by colored dots. Values represent mean ± s.e.m (**$p < 0.01$, ns - non significant difference).

850 **Figure 6: Lesion-induced synaptic plasticity at hippocampal mossy fiber synapses was impaired**
851 **in synaptopodin-deficient tissue cultures.**
852 (A-B) sEPSCs were recorded from dGCs in synaptopodin-deficient tissue cultures (Synpo$^{-/-}$). Here, the
853 mean sEPSC amplitude, half width and area significantly increased 3 days after the ECL (A; $n_{control}$ =
854 29; $n_{3dp\ ECL}$ = 26; Mann-Whitney test; Linear regression fit for XY-plot analysis). In contrast to wildtype
855 cultures, no changes in the mean sEPSC frequency or the sEPSC amplitude/frequency-distribution were
856 observed (B; Mann-Whitney test for column statistics and RM-two-way ANOVA followed by Sidak's
857 multiple comparisons test for XY-plot analysis).
858 (C) No changes in passive membrane properties of dGCs were detected in synaptopodin-deficient
859 cultures upon lesion (Mann-Whitney test for column statistics and RM-two-way ANOVA followed by
860 Sidak's multiple comparisons test for XY-plot analysis).
861 (D-E) The mean sEPSC amplitude in CA3-PCs was not significantly different in lesioned and non-
862 lesioned control cultures. Noteworthy, the mean sEPSC half width significantly decreased in lesioned
863 cultures (D; $n_{control}$ = 25; $n_{3dp\ ECL}$ = 25; Mann-Whitney test; linear regression fit for XY-plot analysis).
864 No lesion-induced changes in the mean sEPSC frequency or the amplitude/frequency-interdependence
865 were detectable (E; Mann-Whitney test for column statistics and RM-two-way ANOVA followed by
866 Sidak's multiple comparisons test for XY-plot analysis).
867 (F) No changes in passive membrane properties of CA3-PCs were detected in synaptopodin-deficient
868 cultures upon lesion (Mann-Whitney test for column statistics and RM-two-way ANOVA followed by
869 Sidak's multiple comparisons test for XY-plot analysis).
870 (G-H) Paired whole-cell patch-clamp recordings were carried out between individual dGCs and CA3-
871 PCs in lesioned and non-lesioned control cultures prepared from synaptopodin-deficient animals (G).
872 Upon injection of 5 current pulses in the presynaptic granule cells, no changes in the pulse-number-
873 dependent response rate of connected mossy fiber synapses were detectable after the ECL (H; $n_{control}$ =
874 12; $n_{3dp\ ECL}$ = 10; Mann-Whitney test for the respective pulse numbers).
875 (I) Analyzing properties of successfully transmitted uEPSCs, a significant decrease in uEPSC amplitude
876 was evident in lesioned cultures when compared to non-lesioned controls ($n°1_{control}$ = 144 events, $n°1_{ECL}$
877 = 82 events; $n°2_{control}$ = 300 events, $n°2_{ECL}$ = 263 events; $n°3_{control}$ = 426 events (one data point outside
878 the axis limits), $n°3_{ECL}$ = 402 events; $n°4_{control}$ = 486 events, $n°4_{ECL}$ = 364 events; $n°5_{control}$ = 472 events,
879 $n°5_{ECL}$ = 317 events; Mann-Whitney test for the respective pulse numbers).

880 Individual data points are indicated by colored dots. Values represent mean ± s.e.m (*$p < 0.05$, ***$p <$
881 0.001, ns - non significant difference).

Figure 7: Synaptopodin deficiency shifted the hippocampal mossy fiber synapse to an excitable state under baseline conditions.

(A-B) sEPSCs from CA3-PCs of both synaptopodin-deficient and wildtype tissue preparations respectively. While the mean sEPSC amplitude was unchanged, sEPSC area and half width were significantly increased in synaptopodin-deficient tissue cultures (A; $n_{Synpo+/+} = 48$; $n_{Synpo-/-} = 25$; Mann-Whitney test; Linear regression fit for XY-plot analysis; c.f., Figures 4 and 6). Additionally, the sEPSC amplitude/frequency-distribution was significantly changed between the two groups (B; RM-two-way ANOVA followed by Sidak's multiple comparisons test).

(C-D) When comparing the response rate of postsynaptic CA3-PCs upon presynaptic action potential generation from paired recordings in $Synpo^{+/+}$ and $Synpo^{-/-}$ tissue preparations, no significant increase was observed (C; $n_{Synpo+/+} = 10$; $n_{Synpo-/-} = 12$; Mann-Whitney test for the respective pulse numbers; c.f., Figures 3 and 6). However, when analyzing the amplitudes of successfully transmitted uEPSCs at the postsynaptic CA3-PCs, a significant increase in uEPSC amplitudes became evident in synaptopodin-deficient tissue preparations after each of the five pulses respectively (D; $n°1_{Synpo+/+} = 20$ events, $n°1_{Synpo-/-} = 144$ events; $n°2_{Synpo+/+} = 115$ events, $n°2_{Synpo-/-} = 300$ events; $n°3_{Synpo+/+} = 292$ events, $n°3_{Synpo-/-} = 426$ events (one data point outside the axis limits); $n°4_{Synpo+/+} = 326$ events, $n°4_{Synpo-/-} = 486$ events; $n°5_{Synpo+/+} = 307$ events, $n°5_{Synpo-/-} = 472$ events; Mann-Whitney test for the respective pulse numbers; c.f., Figures 4 and 6).

Individual data points are indicated by colored dots. Values represent mean ± s.e.m (*$p < 0.05$, **$p < 0.01$, ***$p < 0.001$, ns - non significant difference).

Figure 8: Entorhinal cortex lesion-induced synaptopodin-dependent transcriptomic changes.

(A) Volcano Plots to visualize differential gene expression in wildtype (Synpo$^{+/+}$) and synaptopodin-deficient (Synpo$^{-/-}$) tissue preparations based on region-specific transcriptome analysis of the dentate gyrus (DG) and the CA3 area. Colored dots indicate differentially expressed genes ($p_{adj.} < 0.05$; CA3-Synpo$^{+/+}$: $n_{control} = 2$, $n_{3dpECL} = 3$; DG-Synpo$^{+/+}$: $n_{control} = 4$, $n_{3dpECL} = 7$; CA3-Synpo$^{-/-}$: $n_{control} = 6$, $n_{3dpECL} = 6$; DG-Synpo$^{-/-}$: $n_{control} = 7$, $n_{3dpECL} = 4$; detailed DESeq2-outputs provided in extended data table 8-1, 8-2, 8-3 and 8-4).

(B) VENN-diagrams illustrate the magnitude of lesion-induced differential gene expression and the overlap in commonly regulated genes between wildtype and synaptopodin-deficient tissue preparations. Synaptopodin-deficient preparations showed deficits in lesion-induced gene expression mainly in the CA3 region. Despite the identification of commonly regulated genes, a considerable number of genotype-specific changes can be identified in DG samples.

(C) For wildtype CA3 samples (Synpo$^{+/+}$-CA3), a gene set enrichment analysis (gene ontologies: molecular function (MF) and cellular compartment (CC)) was performed and visualized (TOP-5) by the g:Profiler web platform.

(D) Heatmap-visualization demonstrates the differential expression of synapse related genes (GOCC: 0045202) upon lesion-induced cellular remodeling in the wildtype CA3 region. TOP-10 differentially expressed genes were additionally illustrated.

(E) For wildtype DG samples (Synpo$^{+/+}$-DG), a gene set enrichment analysis (gene ontologies: molecular function (MF) and cellular compartment (CC)) was performed and visualized (TOP-5) by the g:Profiler web platform.

(F) Heatmap-visualization demonstrates the differential expression of synapse related genes (GOCC: 0045202) upon lesion-induced cellular remodeling in the wildtype DG region. TOP-10 differentially expressed genes for both UP and DOWN regulation were additionally illustrated.

Analysis was performed on the Galaxy platform, differential gene expression was determined using the DESeq2 application.

928 **EXTENDED DATA TABLES**

929 Extended data table 5-1: Synaptopodin co-immunoprecipitation experiments (RNA-sequencing results
930 from wildtype co-immunoprecipitation experiments with synaptopodin-KO background control)

931 Extended data table 8-1: DESeq2 results table ECL vs. control (Synpo$^{+/+}$, CA3; Base Mean > 300; c.f.
932 Figure 8)

933 Extended data table 8-2: DESeq2 results table ECL vs. control (Synpo$^{+/+}$, DG; Base Mean > 300; c.f.
934 Figure 8)

935 Extended data table 8-3: DESeq2 results table ECL vs. control (Synpo$^{-/-}$, CA3; Base Mean > 300; c.f.
936 Figure 8)

937 Extended data table 8-4: DESeq2 results table ECL vs. control (Synpo$^{-/-}$, DG; Base Mean > 300; c.f.
938 Figure 8)

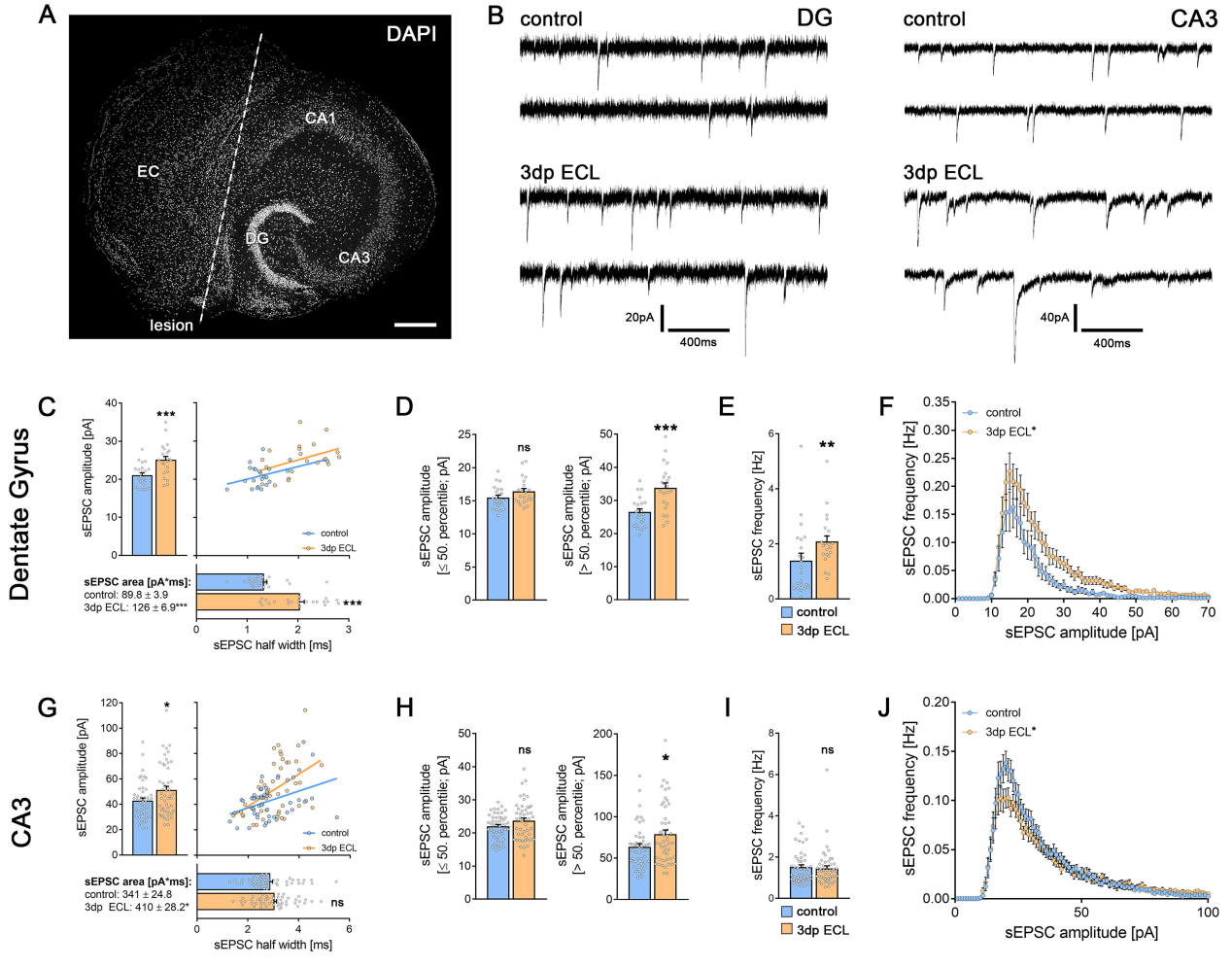
A
DAPI
CA1
EC
DG
CA3
lesion
B
control
DG
3dp ECL
20pA
400ms
control
CA3
3dp ECL
40pA
400ms
Dentate Gyrus
C
sEPSC amplitude [pA]
***
control
3dp ECL
sEPSC area [pA*ms]:
control: 89.8 ± 3.9
3dp ECL: 126 ± 6.9***
***
sEPSC half width [ms]
D
sEPSC amplitude [≤ 50. percentile; pA]
ns
sEPSC amplitude [> 50. percentile; pA]
***
E
sEPSC frequency [Hz]
**
control
3dp ECL
F
control
3dp ECL*
sEPSC frequency [Hz]
sEPSC amplitude [pA]
CA3
G
sEPSC amplitude [pA]
*
control
3dp ECL
sEPSC area [pA*ms]:
control: 341 ± 24.8
3dp ECL: 410 ± 28.2*
ns
sEPSC half width [ms]
H
sEPSC amplitude [≤ 50. percentile; pA]
ns
sEPSC amplitude [> 50. percentile; pA]
*
I
sEPSC frequency [Hz]
ns
control
3dp ECL
J
control
3dp ECL*
sEPSC frequency [Hz]
sEPSC amplitude [pA]

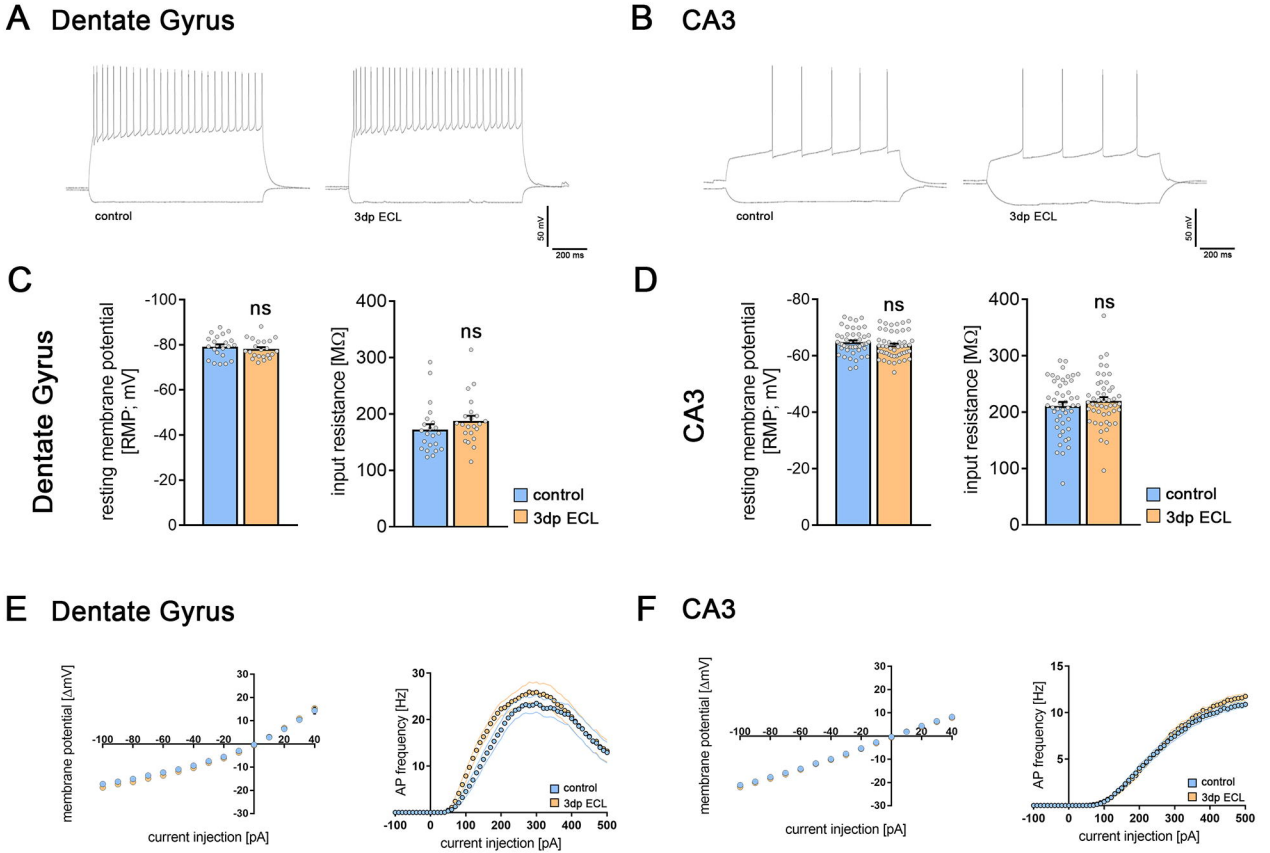
A Dentate Gyrus
control
3dp ECL
50 mV
200 ms
B CA3
control
3dp ECL
50 mV
200 ms
C
Dentate Gyrus
resting membrane potential [RMP; mV]
ns
input resistance [MΩ]
ns
control
3dp ECL
D
CA3
resting membrane potential [RMP; mV]
ns
input resistance [MΩ]
ns
control
3dp ECL
E Dentate Gyrus
membrane potential [ΔmV]
current injection [pA]
AP frequency [Hz]
current injection [pA]
control
3dp ECL
F CA3
membrane potential [ΔmV]
current injection [pA]
AP frequency [Hz]
current injection [pA]
control
3dp ECL

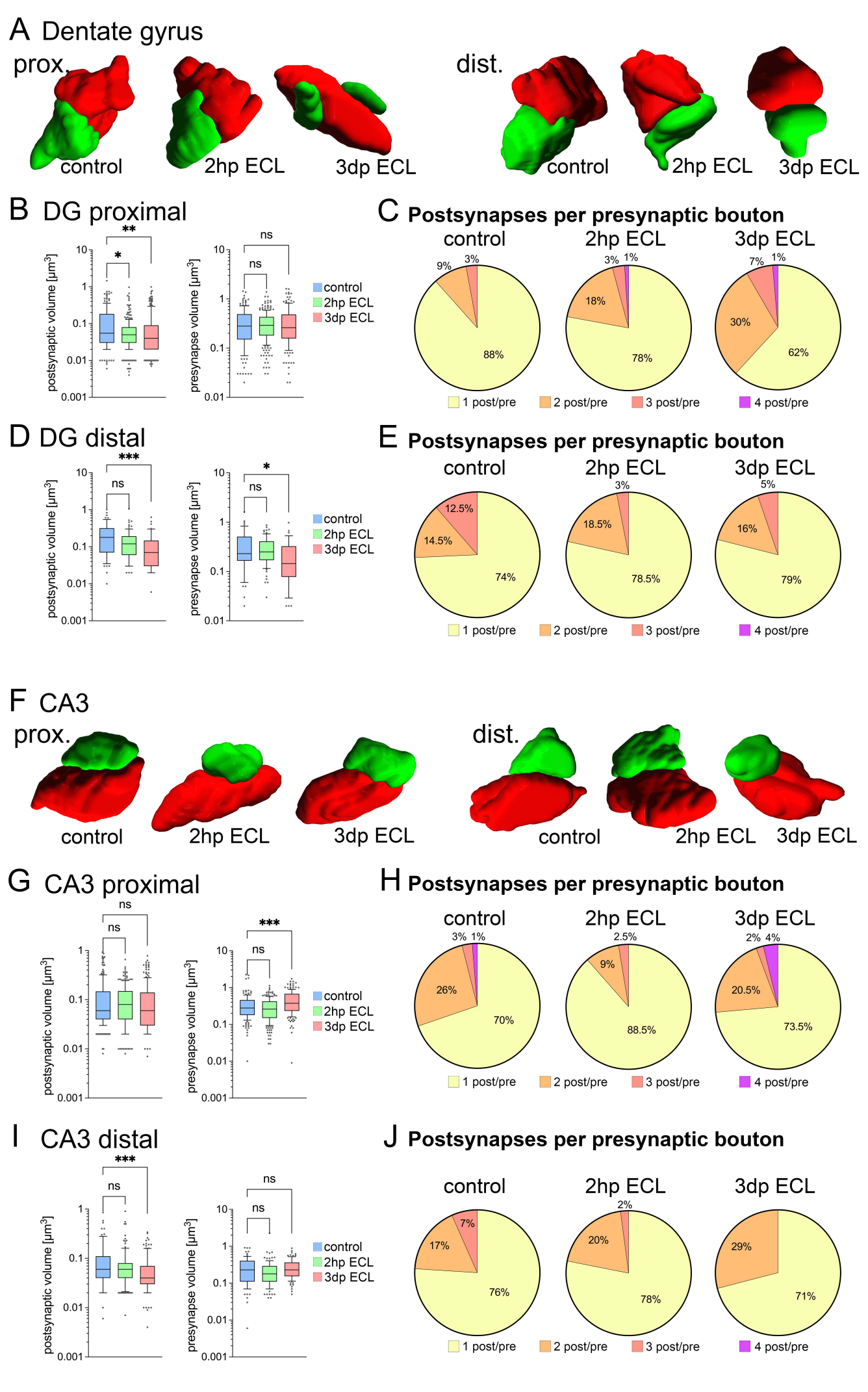
A Dentate gyrus
prox.
control
2hp ECL
3dp ECL
dist.
control
2hp ECL
3dp ECL
B DG proximal
postsynaptic volume [µm³]
presynapse volume [µm³]
**
*
ns
ns
control
2hp ECL
3dp ECL
C Postsynapses per presynaptic bouton
control
2hp ECL
3dp ECL
9%
3%
88%
3%
1%
18%
78%
7%
1%
30%
62%
1 post/pre
2 post/pre
3 post/pre
4 post/pre
D DG distal
postsynaptic volume [µm³]
presynapse volume [µm³]
***
ns
*
ns
control
2hp ECL
3dp ECL
E Postsynapses per presynaptic bouton
control
2hp ECL
3dp ECL
12.5%
14.5%
74%
3%
18.5%
78.5%
5%
16%
79%
1 post/pre
2 post/pre
3 post/pre
4 post/pre
F CA3
prox.
control
2hp ECL
3dp ECL
dist.
control
2hp ECL
3dp ECL
G CA3 proximal
postsynaptic volume [µm³]
presynapse volume [µm³]
ns
ns
***
ns
control
2hp ECL
3dp ECL
H Postsynapses per presynaptic bouton
control
2hp ECL
3dp ECL
3% 1%
26%
70%
2.5%
9%
88.5%
2% 4%
20.5%
73.5%
1 post/pre
2 post/pre
3 post/pre
4 post/pre
I CA3 distal
postsynaptic volume [µm³]
presynapse volume [µm³]
***
ns
ns
ns
control
2hp ECL
3dp ECL
J Postsynapses per presynaptic bouton
control
2hp ECL
3dp ECL
7%
17%
76%
2%
20%
78%
29%
71%
1 post/pre
2 post/pre
3 post/pre
4 post/pre

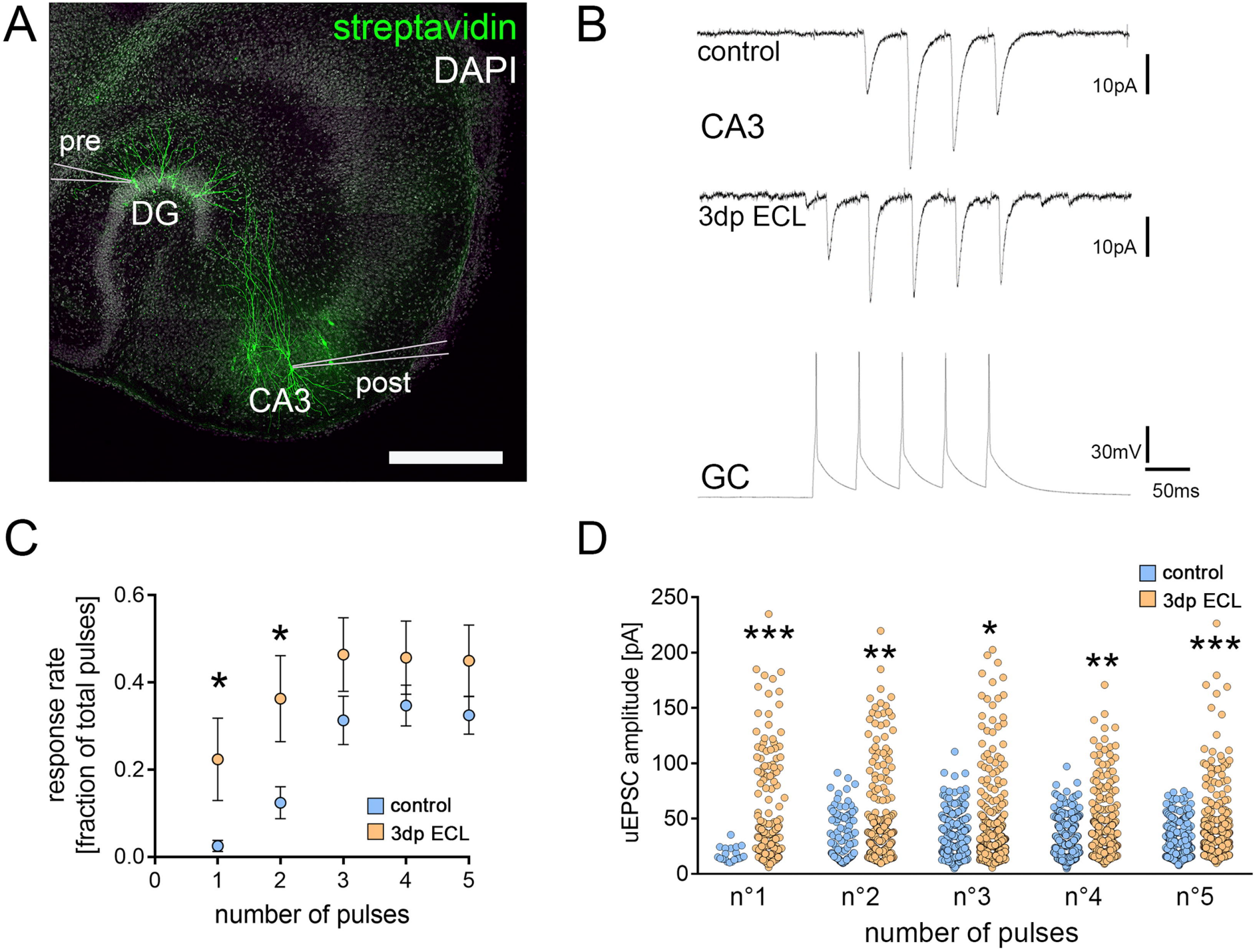
A
streptavidin
DAPI
pre
DG
CA3
post
B
control
10pA
CA3
3dp ECL
10pA
30mV
GC
50ms
C
response rate
[fraction of total pulses]
0.6
0.4
0.2
0.0
0
1
2
3
4
5
number of pulses
*
*
control
3dp ECL
D
control
3dp ECL
uEPSC amplitude [pA]
250
200
150
100
50
0
***
**
*
**
***
n°1
n°2
n°3
n°4
n°5
number of pulses

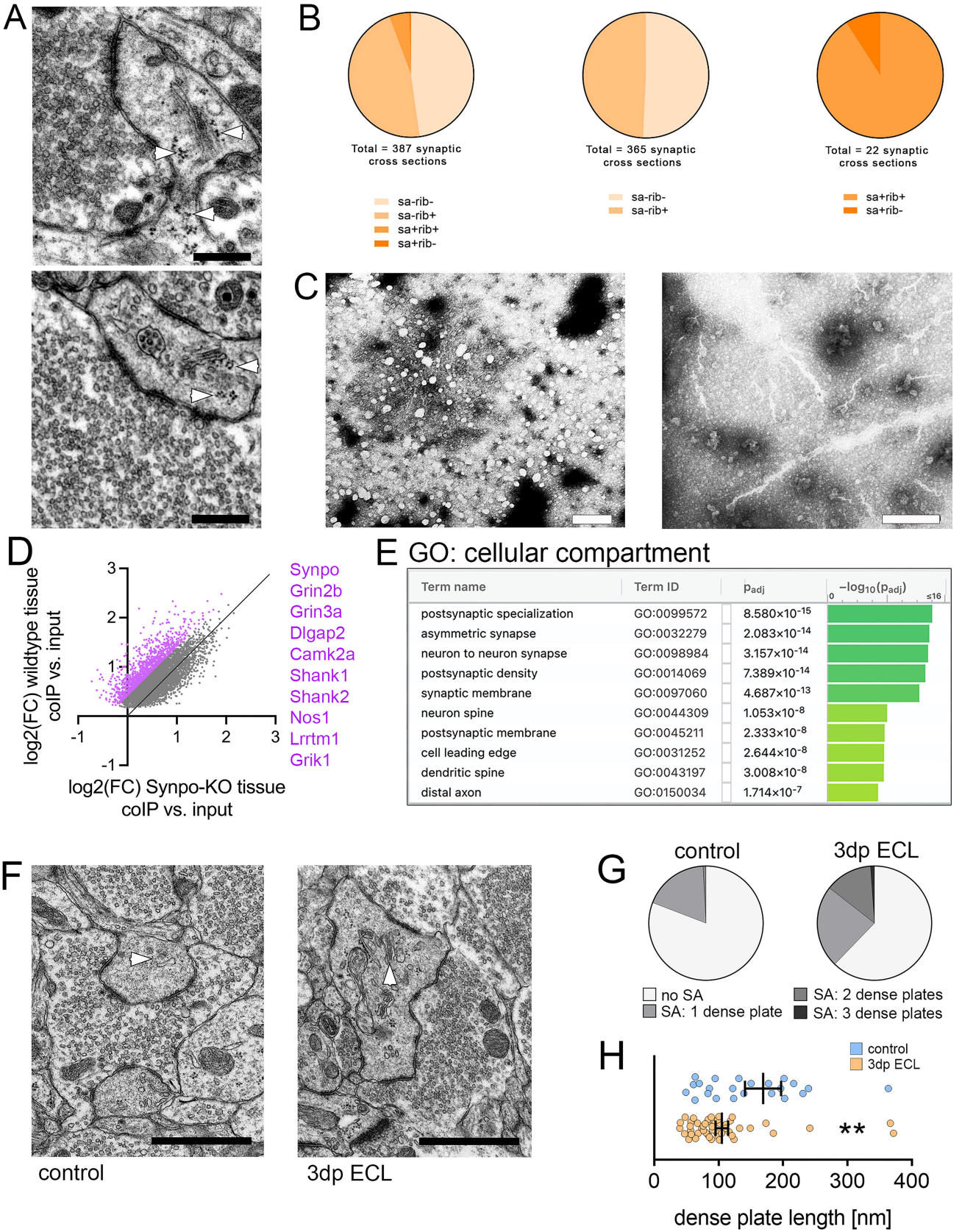
A
B
Total = 387 synaptic cross sections
sa-rib-
sa-rib+
sa+rib+
sa+rib-
Total = 365 synaptic cross sections
sa-rib-
sa-rib+
Total = 22 synaptic cross sections
sa+rib+
sa+rib-
C
D
log2(FC) wildtype tissue coIP vs. input
log2(FC) Synpo-KO tissue coIP vs. input
Synpo
Grin2b
Grin3a
Dlgap2
Camk2a
Shank1
Shank2
Nos1
Lrtm1
Grik1
E
GO: cellular compartment
Term name
Term ID
p_{adj}
$-\log_{10}(p_{adj})$
postsynaptic specialization GO:0099572 8.580×10^{-15}
asymmetric synapse GO:0032279 2.083×10^{-14}
neuron to neuron synapse GO:0098984 3.157×10^{-14}
postsynaptic density GO:0014069 7.389×10^{-14}
synaptic membrane GO:0097060 4.687×10^{-13}
neuron spine GO:0044309 1.053×10^{-8}
postsynaptic membrane GO:0045211 2.333×10^{-8}
cell leading edge GO:0031252 2.644×10^{-8}
dendritic spine GO:0043197 3.008×10^{-8}
distal axon GO:0150034 1.714×10^{-7}
F
control
3dp ECL
G
control
3dp ECL
no SA
SA: 1 dense plate
SA: 2 dense plates
SA: 3 dense plates
H
control
3dp ECL
**
dense plate length [nm]

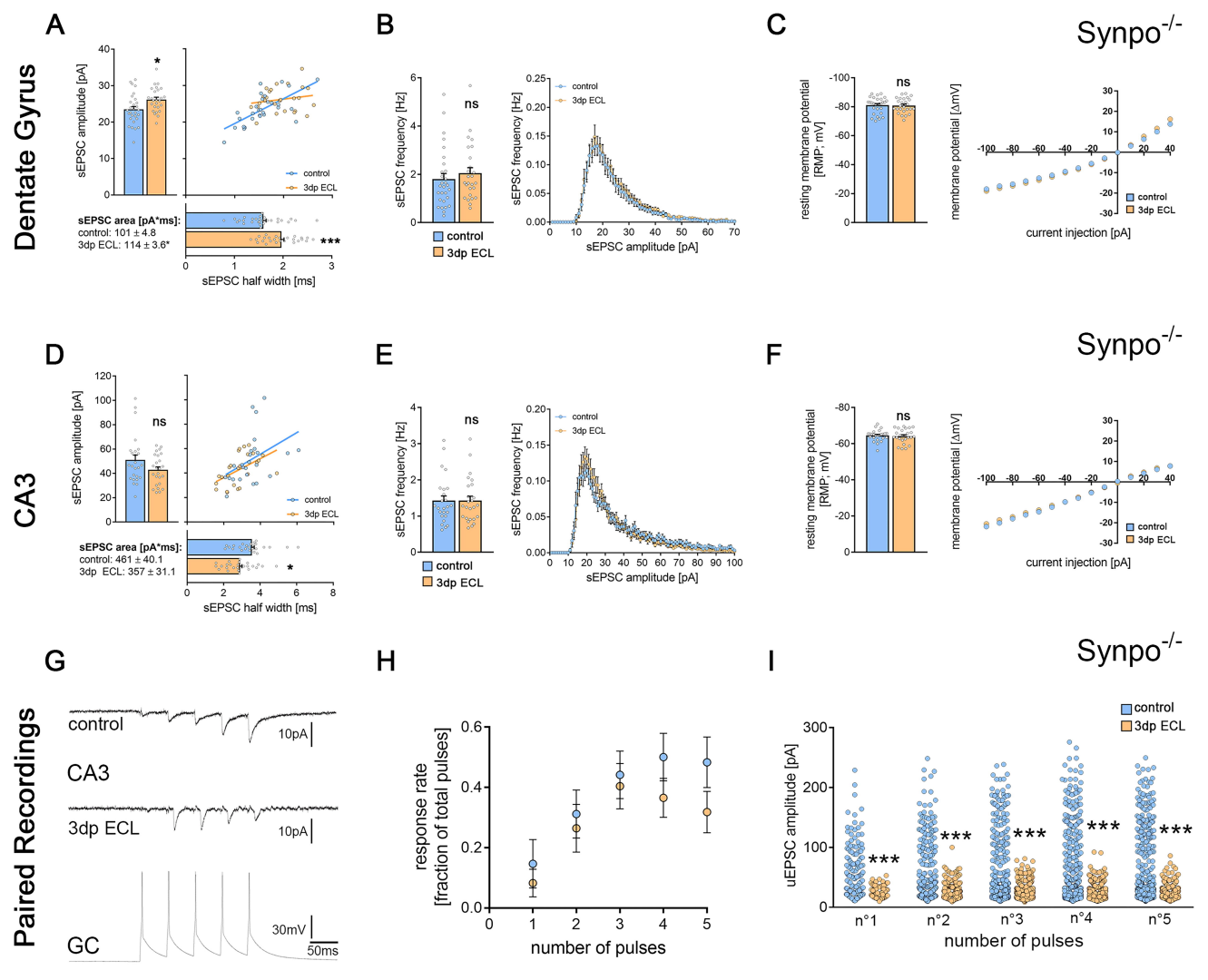
Dentate Gyrus
A
sEPSC amplitude [pA]
control
3dp ECL
sEPSC area [pA*ms]:
control: 101 ± 4.8
3dp ECL: 114 ± 3.6*
sEPSC half width [ms]
B
sEPSC frequency [Hz]
ns
control
3dp ECL
sEPSC amplitude [pA]
C
Synpo-/-
resting membrane potential [RMP; mV]
membrane potential [ΔmV]
current injection [pA]
CA3
D
sEPSC area [pA*ms]:
control: 461 ± 40.1
3dp ECL: 357 ± 31.1
E
F
Paired Recordings
G
control
CA3
3dp ECL
10pA
GC
30mV
50ms
H
response rate [fraction of total pulses]
number of pulses
I
uEPSC amplitude [pA]
n°1
n°2
n°3
n°4
n°5

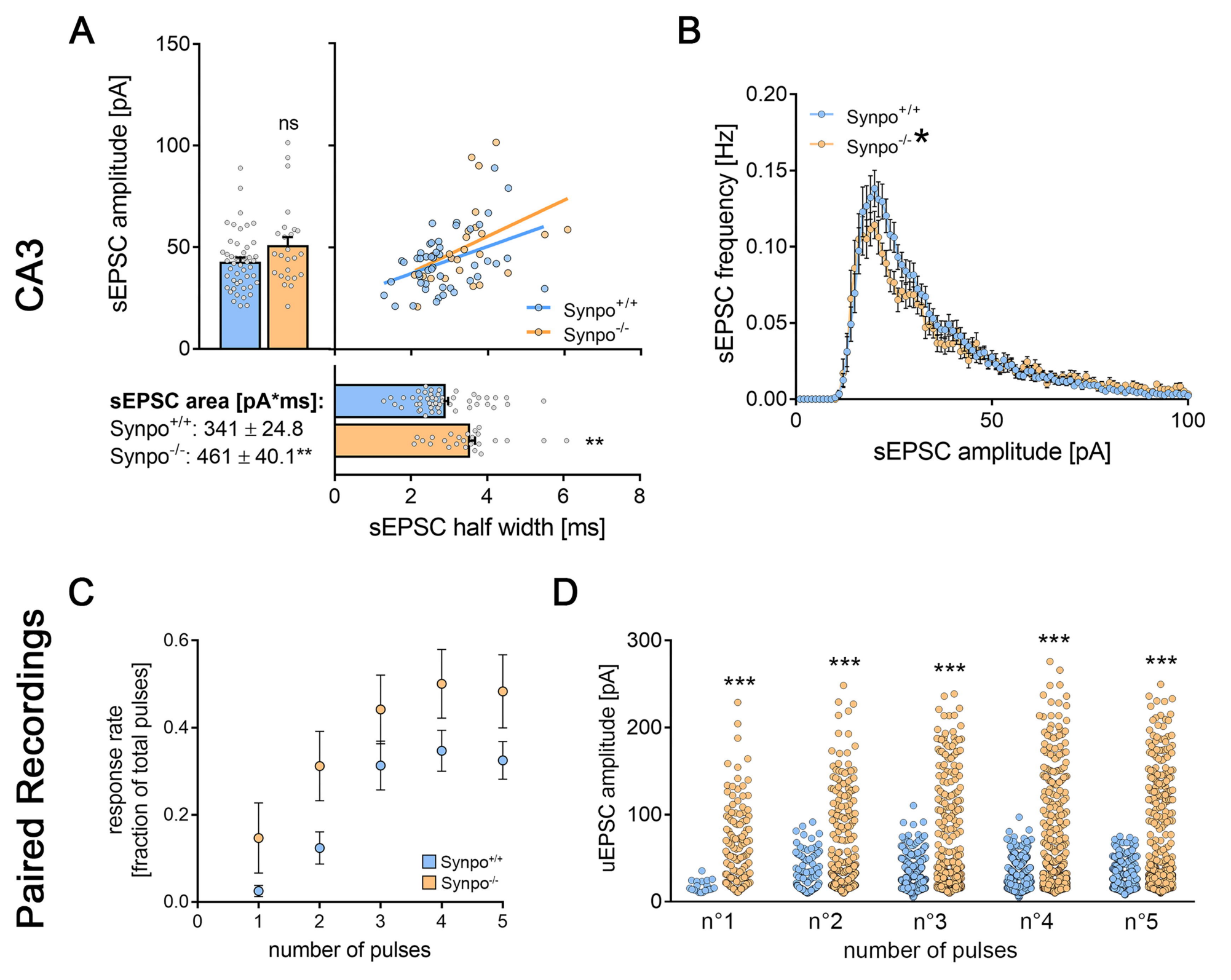
A
CA3
sEPSC amplitude [pA]
150
100
50
0
ns
Synpo+/+
Synpo-/-
sEPSC area [pA*ms]:
Synpo+/+: 341 ± 24.8
Synpo-/-: 461 ± 40.1**
**
0
2
4
6
8
sEPSC half width [ms]
B
sEPSC frequency [Hz]
0.20
0.15
0.10
0.05
0.00
Synpo+/+
Synpo-/-
*
0
50
100
sEPSC amplitude [pA]
C
Paired Recordings
response rate
[fraction of total pulses]
0.6
0.4
0.2
0.0
Synpo+/+
Synpo-/-
0
1
2
3
4
5
number of pulses
D
uEPSC amplitude [pA]
300
200
100
0
***
n°1
n°2
n°3
n°4
n°5
number of pulses

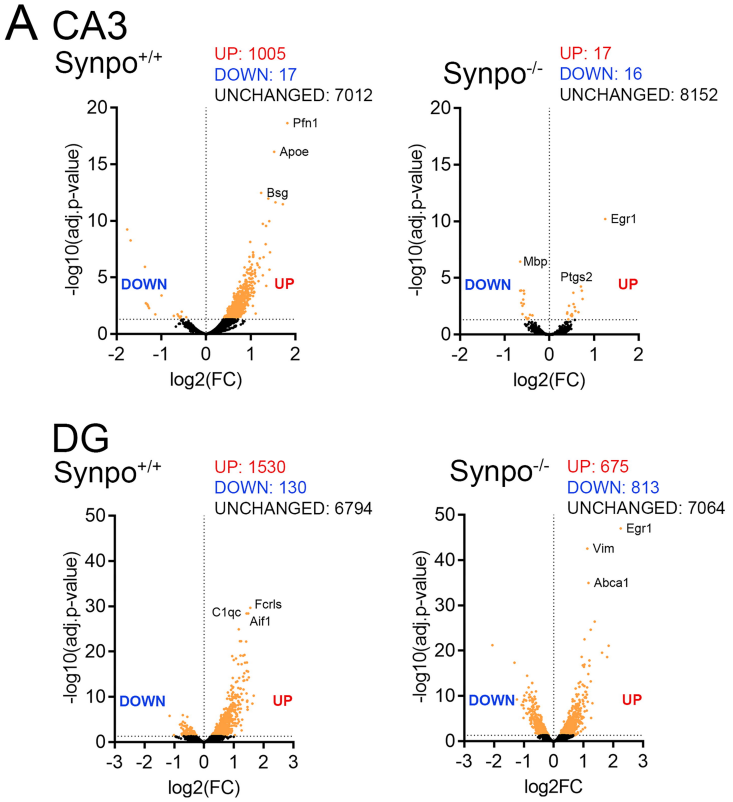

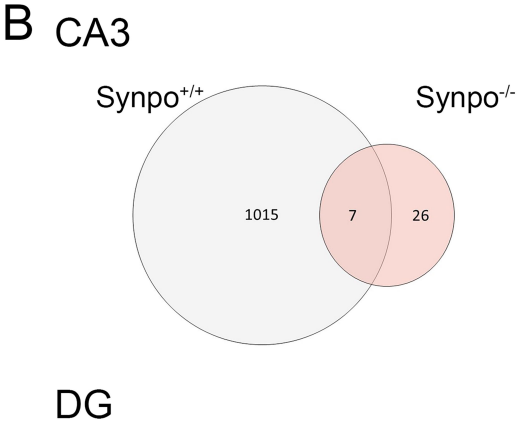

C Synpo+/+ - CA3

GO:MF		stats	
Term name	Term ID	p_{adj}	$-\log_{10}(p_{adj})$
ubiquitin-like protein ligase binding	GO:0044389	2.482×10^{-10}	
ubiquitin protein ligase binding	GO:0031625	6.168×10^{-10}	
GTP binding	GO:0005525	1.490×10^{-8}	
guanyl nucleotide binding	GO:0019001	1.034×10^{-7}	
guanyl ribonucleotide binding	GO:0032561	1.034×10^{-7}	

GO:CC		stats	
Term name	Term ID	p_{adj}	$-\log_{10}(p_{adj})$
exocytic vesicle	GO:0070382	2.324×10^{-19}	
synaptic vesicle	GO:0008021	3.544×10^{-19}	
transport vesicle	GO:0030133	6.265×10^{-19}	
myelin sheath	GO:0043209	3.399×10^{-17}	
glutamatergic synapse	GO:0098978	3.857×10^{-13}	

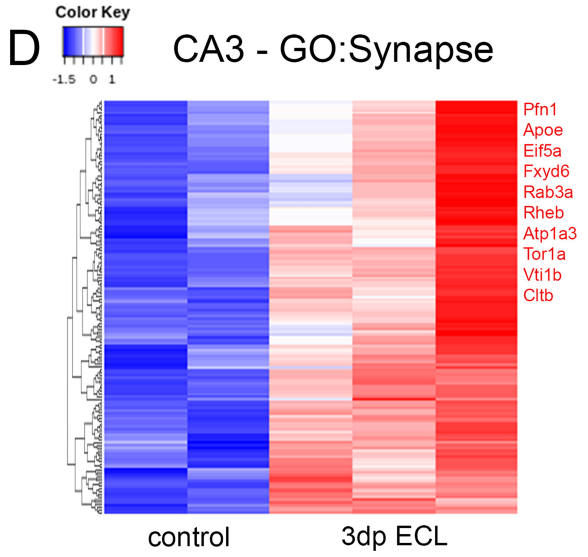

E Synpo+/+ - DG

GO:MF		stats	
Term name	Term ID	p_{adj}	$-\log_{10}(p_{adj})$
actin binding	GO:0003779	1.175×10^{-8}	
ubiquitin-like protein ligase binding	GO:0044389	1.162×10^{-7}	
ubiquitin protein ligase binding	GO:0031625	4.309×10^{-7}	
GTP binding	GO:0005525	4.205×10^{-4}	
DNA-binding transcription factor binding	GO:0140297	9.194×10^{-4}	
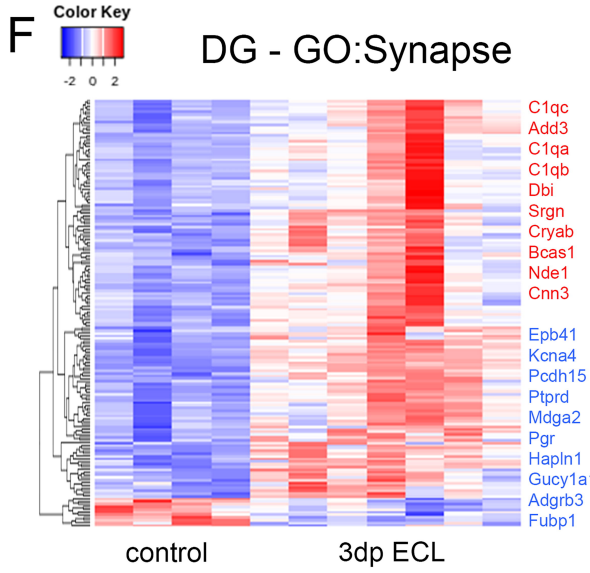
GO:CC		stats	
Term name	Term ID	p_{adj}	$-\log_{10}(p_{adj})$
endosome membrane	GO:0010008	1.049×10^{-12}	
cell leading edge	GO:0031252	5.334×10^{-12}	
mitochondrial matrix	GO:0005759	5.413×10^{-12}	
peptidase complex	GO:1905368	1.144×10^{-11}	
endopeptidase complex	GO:1905369	1.217×10^{-11}